EuroIntervention
2026;22:e44-e54
published online e-edition January 2026
DOI: 10.4244/EIJ-D-25-00671

ORIGINAL RESEARCH

Non-invasive assessment of microcirculatory resistance by coronary computed tomography angiography

Dan Deng[1,2], MD; Ping Zhu[1,2], MD; Xiaolong Qu[1,2], MD; Huakang Li[1,2], MD; Xiaofei Xue[3], MD; Xiujian Liu[3], MD; Zhifan Gao[3], MD; Heye Zhang[3], MD; Haoran Qin[1,2], BSc; Yan Lu[1,2], BSc; Yue Feng[1,2], MSc; Min Zeng[1,2], BSc; Shuhui Chen[1,2], MSc; Xiaolong Li[1,2], BSc; Yang Zhou[1,2], BSc; Feng Liu[1,2], BSc; Hao Gao[1,2], BSc; Wanxiang Zheng[1,2], MSc; Chao Zhang[1,2], BSc; Xiang Xu[1,2], MSc; Wei Chen[4], MD; Dali Yi[5], MD; Giorgos Papanastasiou[6,7], PhD; William Kongto Hau[8], MD; Guang Yang[9], PhD; Zhihui Zhang[1,2]*, MD

D. Deng and P. Zhu contributed equally as first authors.

**Corresponding author: Southwest Hospital of AMU, No. 30, Gaotanyan Main Street, Shapingba District, Chongqing, 400038, China. E-mail: xyzpj@tmmu.edu.cn*

This paper also includes supplementary data published online at: https://eurointervention.pcronline.com/doi/10.4244/EIJ-D-25-00671

ABSTRACT

BACKGROUND: Despite its high prevalence and major prognostic implications, coronary microvascular disease (CMD) is frequently underdiagnosed owing to the complexity and invasiveness of current diagnostic procedures.

AIMS: This study aimed to introduce and validate the usefulness of a non-invasive index of microcirculatory resistance (IMR) derived from coronary computed tomography angiography (CCTA), called IMR_{CT}, for accurate diagnosis of CMD.

METHODS: This retrospective cohort study comprised consecutive patients referred for invasive coronary functional assessments who underwent CCTA within the 30 days preceding an invasive evaluation between January 2022 and March 2024. IMR_{CT} was calculated by blinded evaluators and compared against invasively determined IMR, with IMR values ≥25 indicating CMD, to assess its diagnostic performance.

RESULTS: A total of 176 patients (216 vessels) were included in the analysis. IMR_{CT} showed good correlation with invasively measured IMR, both at the vessel level (r=0.71, 95% confidence interval [CI]: 0.62-0.76; p<0.001) and the patient level (r=0.72, 95% CI: 0.64-0.78; p<0.001). At the vessel level, diagnostic accuracy, sensitivity, specificity, and area under the curve were 81.9%, 80.8%, 82.5%, and 0.82, respectively; corresponding values at the patient level were 80.7%, 81.5%, 80.2%, and 0.81. In patients with non-obstructive coronary artery disease defined by CCTA stenosis <50%, coronary angiogram stenosis <50%, or fractional flow reserve >0.8, IMR_{CT} reduced underdiagnosis rates from 38.8%, 35.3%, and 36.3% to 4.5%, 5.9%, and 5.6%, respectively.

CONCLUSIONS: IMR_{CT} serves as a valuable complement to current diagnostic approaches, addressing their limitations and offering a promising alternative for the diagnosis of CMD, with the potential to significantly reduce misdiagnosis rates.

KEYWORDS: coronary CT angiography; coronary microvascular disease; coronary physiology; index of microcirculatory resistance

SUBMITTED ON 20/06/2025 - REVISION RECEIVED ON 1st 10/08/2025 / 2nd 14/09/2025 - ACCEPTED ON 25/09/2025

Coronary microvascular disease (CMD) represents a clinical condition of myocardial ischaemia resulting from structural and/or functional changes in the coronary microcirculation[1]. Since the pioneering report by Likoff et al on myocardial ischaemia caused by non-obstructive coronary artery disease (CAD)[2], the diagnostic challenges of CMD have become increasingly recognised. Recent studies have demonstrated that up to 60.7% of patients with positive stress tests but non-obstructive CAD have underlying CMD when assessed by the invasive index of microcirculatory resistance (IMR)[3], highlighting a critical gap in current diagnostic approaches.

Unlike obstructive CAD, which is readily identified through anatomical imaging, CMD remains underdiagnosed because of the lack of reliable non-invasive tools[4]. Non-invasive functional tests, including stress echocardiography, positron emission tomography (PET), and cardiac magnetic resonance imaging (MRI), face significant limitations in the comprehensive assessment of coronary microvascular disease[5]. Although PET provides quantitative measurements of myocardial blood flow, its widespread use is hindered by high cost and limited availability. Cardiac MRI, despite offering high spatial resolution, cannot definitively exclude the presence of multivessel epicardial disease. Furthermore, stress echocardiography exhibits operator-dependent variability when assessing coronary flow velocity reserve, which may affect the reproducibility and accuracy of the results.

Although invasive IMR measurements based on thermodilution techniques can effectively diagnose CMD[6-8], their clinical adoption remains limited by procedural risks, costs, and the need for hyperaemic agents. This diagnostic dilemma highlights the urgent need for accurate, non-invasive alternatives to assess coronary microvascular function.

Coronary computed tomography angiography (CCTA) is increasingly recognised for its potential to evaluate microvascular dysfunction through combined anatomical and functional assessment. Recent evidence shows that structural CMD is associated with a 40% reduction in epicardial lumen volume compared to controls ($p<0.001$), with strong correlation to invasive microvascular resistance measurements ($r=-0.59$) and good diagnostic performance (area under the curve [AUC] 0.79)[9]. Significant progress has also been made in applying computational fluid dynamics (CFD) to non-invasive physiological assessment of the coronary circulation, further supporting the feasibility of this integrated approach[10-12]. Building on these advancements, we propose an optimised CCTA-based IMR (IMR_{CT}) measurement method for microvascular evaluation using standard CCTA technology. This approach addresses key limitations of current diagnostic strategies by enabling comprehensive coronary assessment within a single widely available imaging modality.

Editorial, see page e11

Impact on daily practice

This study addresses the unmet need for a reliable, non-invasive diagnostic tool for coronary microvascular disease (CMD) by establishing the clinical utility of a coronary computed tomography angiography-based index of microcirculatory resistance through advanced image-reconstruction technology. The method's simplicity and diagnostic accuracy enhance early CMD detection rates while reducing misdiagnosis, enabling tailored microvascular-targeted therapies. This advancement optimises patient outcomes and refines CMD management strategies by integrating seamlessly into routine cardiovascular imaging workflows.

Methods

STUDY DESIGN AND POPULATION

The study population consisted of consecutive patients retrospectively selected from an academic medical centre between 1 January 2022 and 31 March 2024. The study received ethical approval from the medical ethics review committee (approval number: B KY2024173) and was conducted following the principles of the Declaration of Helsinki. Informed consent was waived by the institutional review board for this retrospective analysis of fully anonymised clinical data, which posed no risk to participants.

Patients who met both of the following criteria were included: (1) successful completion of invasive intracoronary functional assessment for suspected myocardial ischaemia, and (2) availability of CCTA imaging performed within 30 days preceding the invasive procedure. Patients were excluded if they had (1) acute myocardial infarction, (2) incomplete or poor-quality image data, or (3) a history of previous coronary stent implantation or coronary artery bypass grafting.

CCTA IMAGING ACQUISITION

The CCTA protocol adhered to the Society of Cardiovascular Computed Tomography 2021 guidelines[13], using retrospective gating tailored to patient-specific factors such as weight and heart rate/rhythm (voltage 80-120 kV; current 100-350 mA). Imaging covered the coronary arteries, left ventricle, and proximal ascending aorta, achieving optimal resolution and speed with a 0.25 s gantry rotation and 0.6 mm collimation. High-concentration iodine contrast (50-55 mL; 350-370 mg I/mL) was injected at 5.5-6.0 mL/s, optimised for peak enhancement. Slice thickness was set to 0.6 mm; the Bv45 kernel and Advanced Modeled Iterative Reconstruction (ADMIRE [Siemens Healthineers]) algorithm were used for noise reduction and artefact minimisation, respectively. CCTA was performed using a second-generation dual-source computed tomography (CT) system (SOMATOM Definition Flash [Siemens Healthineers]).

Abbreviations

CAD	coronary artery disease	**CMD**	coronary microvascular disease	**IMR**	index of microcirculatory resistance
CCTA	coronary computed tomography angiography	**FFR**	fractional flow reserve	**IMR_{CT}**	CCTA-based index of microcirculatory resistance

INTRACORONARY FUNCTIONAL ASSESSMENT

Coronary angiography was performed using Innova IGS 5 (GE HealthCare). Intracoronary functional measurements were obtained using a non-side hole catheter (6-7 Fr) and a PressureWire X Guidewire (C12009 [Abbott Medical]) equipped with a pressure and temperature sensor, along with a RadiAnalyzer Xpress (St. Jude Medical). The procedures were conducted using established protocols[14].

Before the functional test, 50-200 µg of nitroglycerine was injected. Resting and hyperaemic curves were obtained using three 3 mL saline injections; if the transit time varied by >30%, additional injections were administered until stable measurements were obtained. Maximal hyperaemia was maintained by the continuous infusion of adenosine triphosphate (140-180 µg/kg/min) via a peripheral vein, with simultaneous pressure monitoring. The fractional flow reserve (FFR) was determined as the ratio of distal coronary pressure to aortic pressure during hyperaemia. Coronary flow reserve (CFR) was calculated as the ratio of the mean transit time (Tmn) at rest to the mean transit time during hyperaemia. The IMR was determined as the product of distal coronary pressure and the hyperaemic mean transit time. An FFR ≤0.80, a CFR <2.0, and an IMR ≥25 were considered abnormal[15]. When FFR was ≤0.80, the IMR values were corrected using Yong's formula[16].

ESTIMATION OF IMR_{CT} BASED ON CCTA

The IMR_{CT} calculation method was developed by the Health Information Intelligent Computing Laboratory at the School of Biomedical Engineering, Sun Yat-sen University, Shenzhen, China **(Figure 1, Supplementary Figure 1, Supplementary Figure 2)**. The lab received only CCTA and clinical data without the results of invasive measurements. The lab segmented and reconstructed the coronary arteries, while the clinical centre marked the positions on the reconstructed model based on invasive measurements from coronary angiography.

This method estimates hyperaemic coronary blood flow (CBF) directly from vascular deformation extracted from multiphase CCTA data. Specifically, vascular deformations for each segment were automatically extracted, and inverse problem-solving techniques were applied to implicitly derive CBF. These techniques were based on physical constraints governing the relationship between vascular deformation and coronary blood flow. Segment-specific constraints were enforced, enabling individualised estimation of CBF by ensuring appropriate application of constraints on vascular deformation within each segment.

The estimated hyperaemic CBF served as outlet boundary conditions for subsequent CFD simulations. CFD simulations were then performed on patient-specific coronary artery models, generating pressure and velocity fields. IMR_{CT} values were calculated from these simulation results. In our prior study, we also systematically evaluated the impact of variations in outlet boundary conditions on IMR_{CT} computation[17].

The Tmn prediction and flow estimation algorithm was developed and validated in our previous study, using an independent derivation cohort[17]. In the present study, we applied this established algorithm to a new and independent external validation cohort. The estimated flow was used as the boundary condition for IMR_{CT} calculation. Analysis time was <30 min/case. More details are provided in **Supplementary Appendix 1**[17-22].

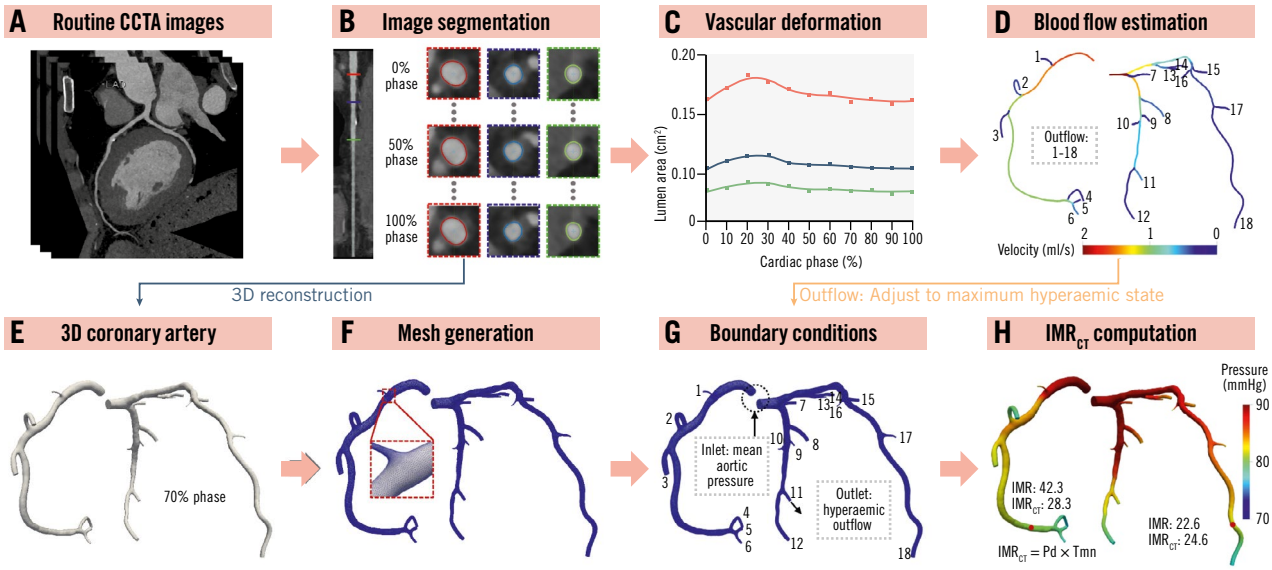

Figure 1. *Overview of the workflow of the proposed IMR_{CT} model. A) Input images of the IMR_{CT} model. B) Segmentation of the multiphase CCTA image. C) Extraction of vascular deformation from the cross-sectional area. D) Coronary blood flow estimation based on vascular deformation. E) 3D model reconstruction of the diastolic coronary artery. F) Mesh generation of the 3D model. G) The setting of inlet and outlet boundary conditions in the CFD simulation. H) The results of IMR_{CT} computation. 3D: three-dimensional; CCTA: coronary computed tomography angiography; CFD: computational fluid dynamics; IMR: index of microcirculatory resistance; IMR_{CT}: CCTA-based IMR; Pd: distal pressure; Tmn: mean transit time*

STATISTICAL ANALYSIS

Shapiro-Wilk and Levene tests were used to assess the normality and homogeneity of variance in the dataset. Continuous variables are presented as the median and interquartile range (first quartile, third quartile). Categorical variables are presented as frequencies and percentages. Pearson and Spearman correlation coefficients evaluated the relationship between IMR_{CT} and invasive IMR, while Bland-Altman analysis assessed agreement. Passing-Bablok regression quantified systematic bias, with the cumulative sum (CUSUM) control chart test confirming linearity. Diagnostic performance was analysed using receiver operating characteristic curves, with accuracy, sensitivity, specificity, positive predictive value, and negative predictive value calculated at patient and vessel levels. Decision curve analysis evaluated clinical utility by comparing the net benefit across risk thresholds. A Sankey diagram was generated to illustrate diagnostic agreement patterns. McNemar's test was used to compare classification differences, and intrapatient vessel variability was assessed using generalised estimating equations. At the patient level, the highest IMR or IMR_{CT} value was used for analysis in cases of multiple vessel measurements. Statistical significance was set at $p<0.05$ (two-tailed test). Analyses were performed using R software, version 4.3.2 (R Foundation for Statistical Computing) and MedCalc software, version 20.215 (MedCalc).

Results

BASELINE CLINICAL CHARACTERISTICS

The study reviewed 324 eligible cases, with 196 having complete examination records. Among these, 20 cases were excluded because of having either incomplete datasets or suboptimal image quality. Consequently, the final analytical sample comprised 176 cases (representing 216 vessels), which were subsequently submitted to the core laboratory for rigorous diagnostic efficacy validation **(Supplementary Figure 3)**.

Table 1 presents the baseline characteristics of the patients (average patient age 61.2±8.8 years; males 65.3%). The median interval between CCTA and invasive IMR measurements was 5 days (interquartile range 4-9 days), with no adverse events occurring between the two examinations.

Supplementary Table 1 presents the distribution of vessels assessed per patient. Among the 176 patients, only 35 (19.9%) underwent IMR measurements in two or three vessels. Of these, 57.1% showed concordant IMR values (either all were above and equal to 25, or all were below 25), while 42.9% demonstrated discordant measurements, revealing myocardial perfusion heterogeneity. Notably, complete three-vessel assessment was performed in just five patients, with three showing consistent IMR values and two exhibiting discordance (illustrated in **Supplementary Figure 4** and **Supplementary Figure 5**, for cases of agreement and disagreement, respectively). This heterogeneity was particularly evident in non-obstructive CAD cases. Among 123 patients with FFR >0.8, 41 (23.3% of the total cohort) showed isolated IMR elevation (CFR ≥2.0 and IMR ≥25), as detailed in **Supplementary Table 2**.

Table 2 shows the characteristics of the 216 vessels included in this study. Among these vessels, 73 (33.8%) had a positive IMR (median IMR 19.5; interquartile range 13.7-29.6).

Table 1. Baseline characteristics of the study population.

Characteristics	N=176
Age, yrs	61.2±8.8
Male	115 (65.3)
Body mass index, kg/m^2	24.5±3.1
Diabetes mellitus	45 (25.6)
Hypertension	113 (64.2)
Current smoker	80 (45.5)
Presence of angina	158 (89.78)
eGFR, mL/min/1.73 m^2	91.5 (78.1, 103.5) (n=175*)
HbA1c, mmol/mol	5.8 (5.5, 6.5) (n=154*)
Total cholesterol, mmol/L	4.2 (3.6, 5.3)
Low-density lipoprotein cholesterol, mmol/L	2.7±0.8
Left ventricular ejection fraction, %	65.0 (61.0, 69.0) (n=169*)
Total calcification score	92.8 (5.6, 341.3) (n=164*)
Interval between CCTA and invasive IMR measurement, days	5.0 (4.0, 9.0)
Number of patients with at least one vessel either >90% stenosed or occluded	26 (14.8)
Nitroglycerine, µg	
50	25 (14.2)
51-100	146 (83.0)
101-200	5 (2.8)
Contrast agent, mL	80.0 (80.0, 110.0)

Values are n (%), mean±standard deviation, or median (interquartile range [Q1, Q3]). *Number of patients for whom continuous variables were calculated. CCTA: coronary computed tomography angiography; eGFR: estimated glomerular filtration rate; HbA1c: glycated haemoglobin; IMR: index of microcirculatory resistance; Q1: first quartile; Q3: third quartile

Notably, only 15 vessels (6.9%) with a positive IMR showed a corresponding positive FFR, while the remaining 58 vessels (26.8%) showed a negative FFR. In the CCTA and coronary angiography reports, 67 (31.0%) and 34 vessels (15.7%) exhibited <50% stenosis, respectively.

DIAGNOSTIC PERFORMANCE OF IMR_{CT} FOR IDENTIFYING CMD

OVERALL DIAGNOSTIC PERFORMANCE

The predicted Tmn was validated against invasively measured Tmn in an independent cohort, showing a strong correlation ($r=0.79$; $p<0.001$) and minimal mean bias (0.05) in Bland-Altman analysis **(Figure 2)**. In our dataset, the optimal AUC value at both patient and vessel levels was achieved at an IMR_{CT} threshold of 23.84. At the vessel level, this threshold yielded the following values: AUC 0.85 (95% confidence interval [CI]: 0.80-0.90), accuracy 81.0% (95% CI: 75.1-86.0%), sensitivity 87.7% (95% CI: 77.9-94.2%), and specificity 77.6% (95% CI: 69.9-84.2%). The corresponding patient-level values were as follows: AUC 0.86 (95% CI: 0.80-0.91), accuracy 80.1% (95% CI: 73.4-85.7%), sensitivity 89.2% (95% CI: 79.1-95.6%), and specificity 74.8% (95% CI: 65.6-82.5%).

Table 2. Coronary artery characteristics.

Characteristics	216 vessels
Vessel	
LM	0 (0)
LAD	135 (62.5)
LCx	32 (14.8)
RCA	49 (22.7)
TIMI flow grade	
TIMI 3	205 (94.9)
TIMI 1 or TIMI 2	11 (5.1)
FFR	0.86 (0.80, 0.91)
IMR	19.5 (13.7, 29.6)
CFR	3.2 (2.3, 4.8)
IMR_{CT}	21.7 (14.8, 28.6)
Diameter of stenosis based on CCTA, %	
<50%	67 (31.0)
50-69%	92 (42.6)
70-90%	57 (26.4)
Diameter of stenosis based on CAG, %	
<50%	34 (15.7)
50-69%	125 (57.9)
70-90%	57 (26.4)
Vessels with FFR >0.8	160 (74.1)
Vessels with IMR ≥25	73 (33.8)
Vessels with IMR_{CT} ≥25	84 (38.9)
Vessels with FFR ≤0.8 and IMR ≥25	15 (6.9)
Vessels with FFR ≤0.8 and IMR <25	41 (19.0)
Vessels with FFR >0.8 and IMR ≥25	58 (26.8)
Vessels with FFR >0.8 and IMR <25	102 (47.2)

Values are presented as n (%) or median (interquartile range [Q1, Q3]). CAG: coronary angiography; CCTA: coronary computed tomography angiography; CFR: coronary flow reserve; FFR: fractional flow reserve; IMR: index of microcirculatory resistance; IMR_{CT}: CCTA-based IMR; LAD: left anterior descending artery; LCx: left circumflex artery; LM: left main artery; Q1: first quartile; Q3: third quartile; RCA: right coronary artery; TIMI: Thrombolysis in Myocardial Infarction

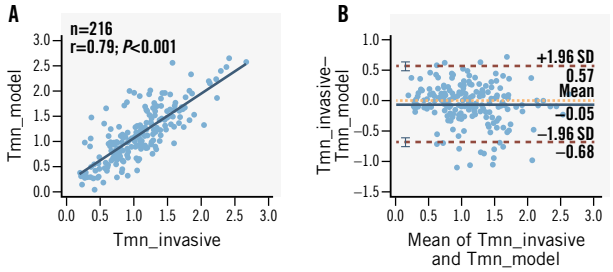

Figure 2. *Correlation and agreement between the Tmn calculated by the IMR_{CT} model and the invasive Tmn. A) Correlation between predicted and invasively measured Tmn. B) Bland-Altman plot of predicted versus invasively measured Tmn. CT: computed tomography; IMR_{CT}: CCTA-based index of microcirculatory resistance; SD: standard deviation; Tmn: mean transit time*

However, the low specificity necessitated additional adjustments. To balance sensitivity and specificity while improving understanding, acceptance, decision-making, and result interpretation, we re-evaluated the IMR_{CT} using a threshold of 25, consistent with the threshold for the IMR. At this threshold, IMR_{CT} showed vessel-level accuracy, sensitivity, and specificity of 81.9% (95% CI: 76.2-86.8%), 80.8% (95% CI: 69.9-89.1%), and 82.5% (95% CI: 75.3-88.4%), respectively **(Table 3)**. Similarly, at the patient level, the predictive accuracy, sensitivity, and specificity were 80.7% (95% CI: 74.1-86.0%), 81.5% (95% CI: 70.0-90.1%), and 80.2% (95% CI: 71.5-87.1%), respectively **(Table 3)**. With a cutoff value of 25, the vessel- and patient-level AUCs for predicting IMR ≥25 were 0.82 (95% CI: 0.76-0.87) and 0.81 (95% CI: 0.74-0.86), respectively **(Figure 3A, Figure 3B)**. Thus, a cutoff value of 25 for IMR_{CT} increased specificity while preserving adequate sensitivity and was particularly beneficial in terms of clinical applicability, reliability, and user-friendliness. Interestingly, although this cutoff value did not yield the highest AUC, it demonstrated greater accuracy than a cutoff value of 23.84. Therefore, we set the IMR_{CT} cutoff at 25 in our study. Detailed vessel- and patient-level classifications are provided in **Supplementary Table 3**.

A notable linear correlation was observed between IMR_{CT} and invasively measured IMR, with correlation coefficients of 0.71 at the vessel level (95% CI: 0.62-0.76; p<0.001) and 0.72 at the patient level (95% CI: 0.64-0.78; p<0.001), as shown in **Figure 3C** and **Figure 3D**. Passing-Bablok regression analysis between the IMR_{CT} and the invasive IMR at the patient level **(Supplementary Figure 6)** yielded the following equation:

$$IMR = -3.02 + 1.14 \times IMR_{CT}$$

indicating a small systematic difference (intercept: –3.02, 95% CI: –5.90 to –0.59) and a proportional bias (slope: 1.144, 95% CI: 1.030 to 1.275). The CUSUM test for linearity (p=0.40) confirmed the appropriateness of the linear model. Bland-Altman analysis further demonstrated small mean biases of 0.78 (95% CI: –0.43 to 2.01) and 0.92 (95% CI: –0.45 to 2.29) at the vessel and patient levels, respectively **(Figure 3E, Figure 3F)**. The Sankey diagram **(Figure 4)** illustrates the diagnostic performance of IMR_{CT}, with correct classification in 81.9% of cases (59 true positives and 118 true negatives) and discordant results in

Table 3. Diagnostic efficacy of IMR_{CT} at vessel and patient levels for IMR ≥25.

	No.	IMR ≥25	Accuracy	Sensitivity	Specificity	PPV	NPV	AUC
Vessel level	216	73 (33.8)	81.9 (76.2-86.8)	80.8 (69.9-89.1)	82.5 (75.3-88.4)	70.3 (61.9-77.4)	89.4 (84.0-93.1)	0.82 (0.76-0.87)
Patient level	176	65 (36.9)	80.7 (74.1-86.0)	81.5 (70.0-90.1)	80.2 (71.5-87.1)	70.7 (62.0-78.1)	88.2 (81.5-92.6)	0.81 (0.74-0.86)

The values are presented as n (%) or % (95% confidence interval). AUC: area under the curve; IMR: index of microcirculatory resistance; IMR_{CT}: coronary computed tomography angiography-based IMR; NPV: negative predictive value; PPV: positive predictive value

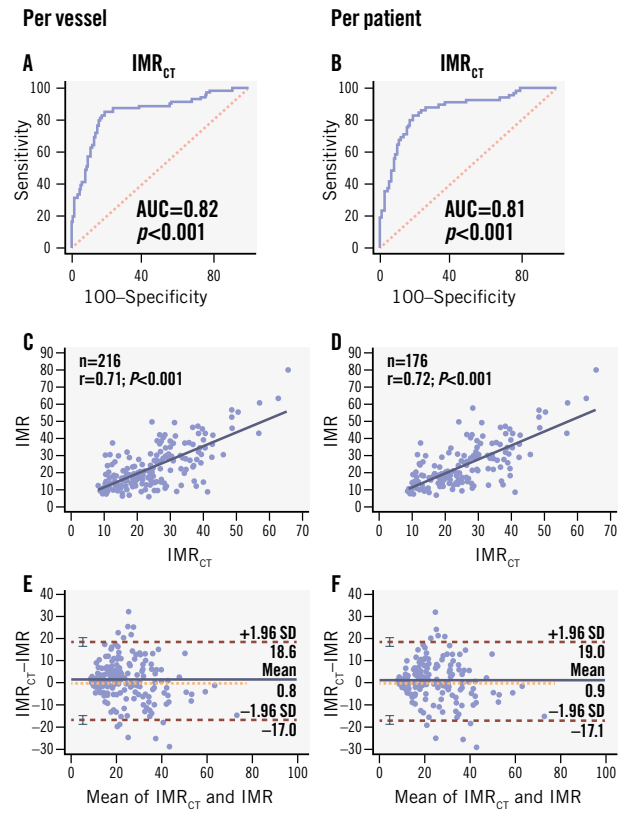

Figure 3. *Per-vessel and per-patient diagnostic performance of IMR_{CT}. A, B) AUC of IMR_{CT} to IMR; (C, D) correlation of IMR_{CT} to IMR; (E, F) Bland-Altman plots of IMR_{CT} and IMR. AUC: area under the curve; IMR: index of microcirculatory resistance; IMR_{CT}: coronary computed tomography angiography-based IMR; SD: standard deviation*

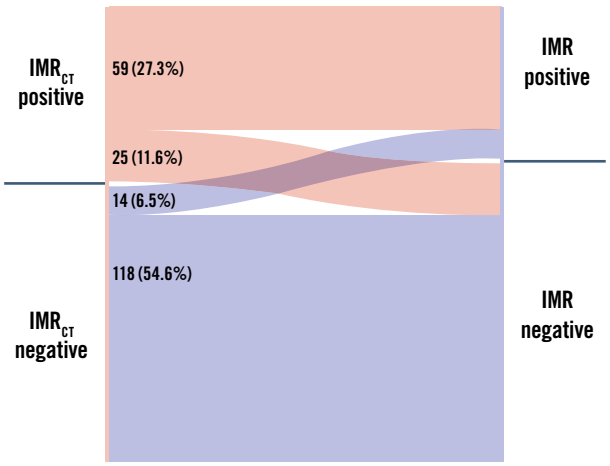

Figure 4. *Sankey diagram of diagnostic agreement between IMR_{CT} and IMR for CMD assessment. The Sankey diagram illustrates the counts and proportions of agreement and disagreement between IMR_{CT} and IMR classifications. Each coloured segment corresponds to a specific category, with its width indicating the number of cases. The transitions between categories highlight patterns of diagnostic misclassification and provide insights into the performance of both methods. CMD: coronary microvascular disease; IMR: index of microcirculatory resistance; IMR_{CT}: coronary computed tomography angiography-based IMR*

18.1% (25 false positives and 14 false negatives). The McNemar test revealed non-significant differences at both the vessel level (5.09%, 95% CI: –0.53% to 10.72%; p=0.108) and the patient level (5.68%, 95% CI: –0.76% to 12.12%; p=0.121).

Supplementary Figure 7 illustrates IMR_{CT} computation under four physiological scenarios: FFR-positive and IMR-positive, FFR-positive and IMR-negative, FFR-negative and IMR-positive, and FFR-negative and IMR-negative.

FUNCTIONAL PHENOTYPES AND SUBGROUP PERFORMANCE ANALYSES

The diagnostic performance of IMR_{CT} was evaluated across key clinical and anatomical subgroups. Analysis of coronary physiology phenotypes **(Supplementary Table 2)** revealed four distinct patterns: normal microvascular function (CFR ≥2.0 and IMR <25) in 65 cases (36.9%), isolated IMR elevation (CFR ≥2.0 and IMR ≥25) in 41 cases (23.3%), mixed microvascular dysfunction (CFR <2.0 and IMR ≥25) in 9 cases (5.1%), and functional CMD (CFR <2.0 and IMR <25) in 8 cases (4.5%). Sex-specific analysis showed isolated IMR elevation was more prevalent in females (26.2%, 16/61) than males (21.7%, 25/115), while functional CMD showed the opposite pattern (females 3.3% [2/61] vs males 5.2% [6/115]).

The diagnostic accuracy of IMR_{CT} showed sex-specific differences, with higher performance in males (86.2%, 95% CI: 77.5-92.4%) compared to females (78.7%, 95% CI: 70.2-92.3%). Accuracy remained comparable between hypertensive (82.0%) and non-hypertensive patients (81.8%), as well as between subgroups of diabetic (81.3%) and non-diabetic patients (82.7%) **(Supplementary Table 4, Supplementary Table 5)**.

When analysed by coronary territory, IMR_{CT} demonstrated the highest accuracy in the right coronary artery (RCA; 87.8%; 95% CI: 75.2-95.4%), followed by the left circumflex (LCx; 84.4%; 95% CI: 67.2-94.7%) and left anterior descending arteries (LAD; 79.3%; 95% CI: 71.4-85.8%), as detailed in **Supplementary Table 6** and **Supplementary Table 7**.

EVALUATING THE POTENTIAL OF IMR_{CT} IN REDUCING MISDIAGNOSIS ACROSS DIVERSE SUBGROUPS

Since only a few patients underwent IMR measurements in all three vessels, patient-level analysis may have underestimated diagnostic omissions. Therefore, we used vessel-level analysis to accurately assess undetected cases, aiming to gauge the potential of IMR_{CT} in reducing diagnostic oversights in the absence of IMR assessment. In every scenario, the use of IMR_{CT} reduced the initial misdiagnosis rate, as detailed in **Table 4**. Notably, in patients classified as having non-obstructive CAD based on CCTA stenosis <50%, coronary angiography stenosis <50%, or FFR >0.8, the use of IMR_{CT} significantly reduced the initial rates of underdiagnosis from 38.8%, 35.3%, and 36.3% to 4.5%, 5.9%, and 5.6%, respectively.

Table 4. Assessment of potential misdiagnosis and alterations post-IMR_{CT} implementation across diverse scenarios.

Clinical scenarios (n)	Vessels with IMR ≥25	Initial misdiagnosis, %	Vessels correctly identified by IMR_{CT}	Post-IMR_{CT} misdiagnosis, %
CCTA stenosis <50% (67)	26	38.8	23	4.5
CCTA stenosis ≥50% (149)	47	31.5	36	7.4
CAG stenosis <50% (34)	12	35.3	10	5.9
CAG stenosis ≥50% (182)	61	33.5	49	6.6
FFR >0.8 (160)	58	36.3	49	5.6
FFR ≤0.8 (56)	15	26.8	10	8.9

The miss rate refers to the proportion of IMR-positive cases within their respective subgroups. CAG: coronary angiography; CCTA: coronary computed tomography angiography; FFR: fractional flow reserve; IMR: index of microcirculatory resistance; IMR_{CT}: CCTA-based IMR

DECISION CURVE ANALYSIS FOR CLINICAL UTILITY ASSESSMENT

Decision curve analysis of the IMR_{CT}-based predictive model **(Supplementary Figure 8)** demonstrated its superior clinical utility, with the model's net benefit **(Supplementary Figure 8A)** nearly consistently exceeding both the "treat all" and "treat none" strategies. The model maintained robust performance across varying clinical scenarios, as shown in **Supplementary Figure 8B** where the number of true high-risk patients (dashed blue line) declined more gradually than the total high-risk classifications (solid red line) with increasing cost-benefit ratios (range: 1:100 to 100:1), confirming its ability to preserve diagnostic accuracy under more stringent criteria while appropriately reducing unnecessary interventions.

Discussion

To our knowledge, this is the first CT angiography-based method for evaluating coronary microcirculation. The IMR_{CT} demonstrated good correlation with invasively determined measurements at both the vessel (r=0.71, 95% CI: 0.62-0.76; p<0.001) and patient (r=0.72, 95% CI: 0.64-0.78; p<0.001) levels, achieving diagnostic accuracies of 81.9% and 80.7%, respectively. Thus, IMR_{CT} represents a reliable, non-invasive tool for diagnosing coronary microvascular disease. Given the widespread availability of CCTA, IMR_{CT} holds significant clinical implications **(Central illustration)**.

IMR_{CT} CAN OVERCOME THE LIMITATIONS OF CURRENT FUNCTIONAL ASSESSMENTS FOR CMD

IMR_{CT} analysis uses multiphase CCTA data from routine clinical scans with retrospective electrocardiogram gating, eliminating the need for additional scans. This approach allows the seamless integration of non-invasive IMR_{CT} assessments into clinical practice while prioritising patient safety.

With sensitivities and specificities of approximately 80% in comparison with invasive IMR measurements, IMR_{CT} may be suitable for broader clinical adoption. Our findings were systematically compared with established functional measurement techniques. A recent meta-analysis demonstrated that angiography-derived IMR achieved diagnostic parameters of 81% sensitivity, 80% specificity, and an AUC of 0.868[23]. Although IMR_{CT} provides similar diagnostic accuracy, its non-invasive nature represents a distinct clinical advantage. An apparent discrepancy warrants discussion: while Passing-Bablok regression indicated systematic underestimation of invasive IMR by IMR_{CT} (slope B=1.144) **(Supplementary Figure 6)**, the Sankey diagram revealed a higher rate of false positives (11.6%) than false negatives (6.5%) **(Figure 4)**. This paradox can be explained by fundamental differences between these analytical approaches.

First, the continuous nature of regression analysis captures absolute measurement differences across the full range of values, whereas classification-based analysis depends strictly on threshold-defined categories (IMR ≥25). Second, IMR_{CT} exhibits greater variability near the diagnostic cutoff – likely due to limitations in CT spatial resolution and inherent haemodynamic fluctuations during measurement – resulting in more frequent misclassification of true-negative cases, despite overall lower absolute values. Notably, decision curve analysis confirmed that these technical discrepancies have minimal clinical impact **(Supplementary Figure 8)**, as IMR_{CT} demonstrated consistently superior net benefit across all risk thresholds. This suggests that most misclassifications occur in clinically ambiguous cases, where either diagnostic call would have little influence on clinical management.

Subgroup analyses revealed important patterns in IMR_{CT} performance. While showing consistent accuracy across subgroups of patients with hypertension and diabetes, IMR_{CT} demonstrated reduced diagnostic performance in females and in the left anterior descending artery (likely owing to its anatomical complexity[24]). Sex-specific analysis revealed females had a higher prevalence of isolated IMR elevation (26.2% vs 21.7% in males) but lower rates of strictly defined functional CMD (CFR <2.0 and IMR <25; 3.3% vs 5.2%). These distinct sex-based patterns reflect well-established differences in microvascular pathophysiology, the underlying mechanisms of which warrant further investigation[25-27].

We acknowledge that while IMR_{CT} provides reliable resistance measurement, comprehensive CMD evaluation requires both resistance-based (IMR) and flow-based (CFR) metrics. Our data reveal important diagnostic discrepancies when these metrics are combined: 23.3% of patients exhibited isolated IMR elevation (CFR ≥2.0 with IMR ≥25), while 4.5% showed isolated CFR impairment (CFR <2.0 with IMR <25) **(Supplementary Table 2)**. These patterns likely reflect distinct pathophysiological mechanisms – the former suggesting microvascular remodelling or focal resistance abnormalities and the latter indicating global flow impairment due to endothelial dysfunction or diffuse disease. This validation

EuroIntervention — Central Illustration

Diagnostic performance and merits of IMR_{CT} in CMD.

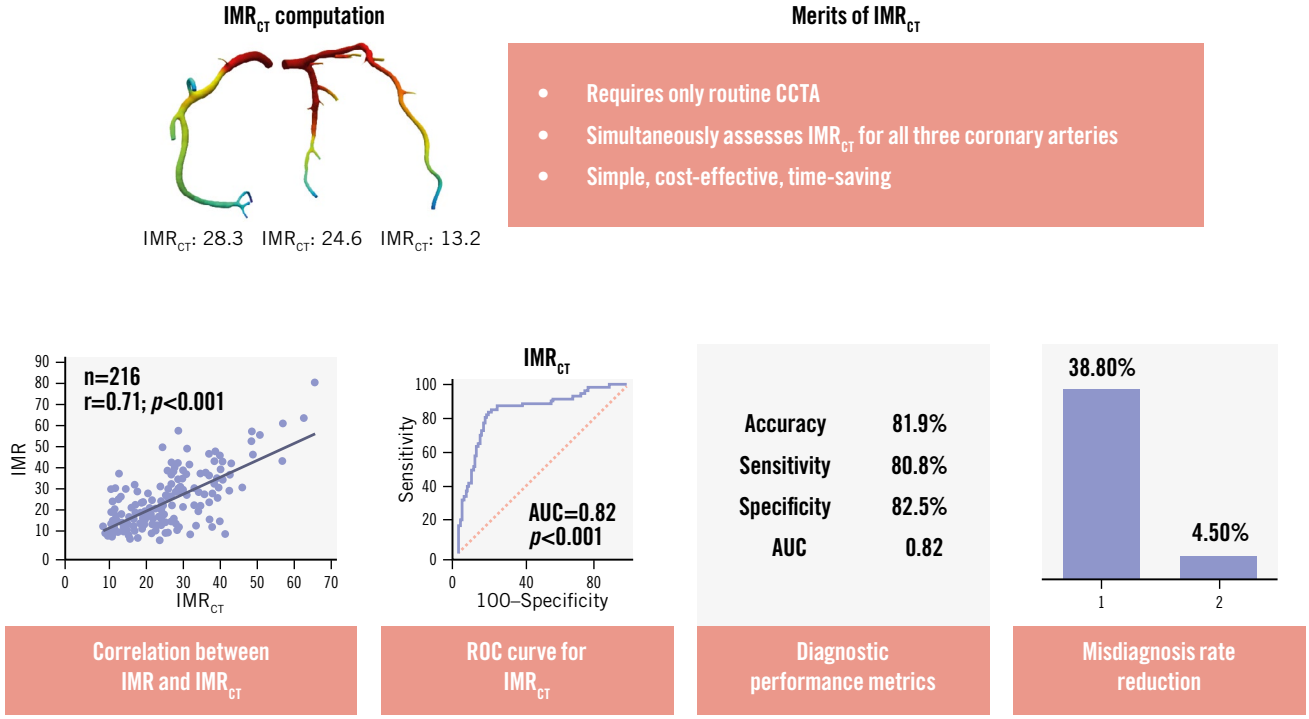

Dan Deng *et al.* • *EuroIntervention* 2026;22:e44-e54 • DOI: 10.4244/EIJ-D-25-00671

IMR_{CT} leverages routine CCTA to provide an accurate, non-invasive approach for CMD diagnosis, markedly reducing missed diagnoses and overcoming the limitations of conventional methods. AUC: area under the curve; CCTA: coronary computed tomography angiography; CMD: coronary microvascular disease; IMR: index of microcirculatory resistance; IMR_{CT}: CCTA-based IMR; ROC: receiver operating characteristic

study was intentionally designed to evaluate IMR_{CT} against invasive IMR, positioning it as a complementary tool rather than a complete substitute for existing diagnostics. The observed discrepancies between IMR and CFR measurements underscore why neither metric alone suffices for comprehensive CMD assessment. Our approach proves particularly valuable for the clinically relevant subgroup with isolated IMR elevation, though we recognise that patients with discordant CFR/IMR findings (e.g., preserved IMR with low CFR) represent a diagnostic gap for IMR_{CT} in its current form.

While some evidence suggests better outcomes for patients with isolated IMR elevation compared to those with combined abnormalities, their long-term prognosis requires further study. Notably, our data show that 38% of vessels with FFR >0.8 had abnormal IMR but normal CFR, highlighting how IMR_{CT} could detect early microvascular disease missed by flow-based assessments alone. Emerging CT-based CFR techniques may soon enable fully non-invasive multimodal assessment when combined with IMR_{CT}, potentially resolving these diagnostic discrepancies by capturing both resistance and flow components of CMD pathophysiology.

IMR_{CT} CAN MITIGATE THE UNDERDIAGNOSIS OF CMD ACROSS DIVERSE CLINICAL SCENARIOS

CMD accounts for 28% to 43% of chest pain cases with non-obstructive CAD[28] and shows a comorbidity rate of 41%[29]. Vessels showing <50% stenosis on CCTA/coronary angiography or FFR >0.8 are considered low risk and often not tested further. In our study, many of these vessels showed positive invasive IMR results, indicating missed CMD diagnoses, and IMR_{CT} substantially reduced these missed diagnoses. Thus, IMR_{CT} can decrease CMD underdiagnosis rates in non-obstructive CAD. Early diagnosis and tiered management of CMD can significantly improve angina symptoms and quality of life[30]. Since clinicians often tend to focus on major epicardial vessel lesions, potentially overlooking concurrent microvascular disease, IMR_{CT} can help identify coexisting CMD in patients with obstructive CAD (CCTA/coronary angiography stenosis ≥50% or FFR ≤0.8).

IMR_{CT} CAN YIELD NON-INVASIVE ASSESSMENTS OF ALL MAJOR CORONARY ARTERIES

To assess the overall microcirculatory condition of the myocardium, IMR measurements of all three major coronary arteries are necessary. In the 3V FFR-FRIENDS study[31], among

patients undergoing three-vessel IMR evaluation, 59.1% had no CMD, while 23.7% had CMD in one vessel, 14.0% in two vessels, and 3.2% in all three vessels. Moreover, the incidence of CMD was similar across the LAD, LCx, and RCA[32].

The 3V FFR-FRIENDS study[31] enrolled patients with >30% stenosis in all three coronary arteries, but in real-world clinical practice, patients often show a combination of stenotic and non-stenotic vessels. Ethical concerns limit invasive examinations to stenotic or slow-flow vessels, often the LAD. In our study, we analysed 135 LAD, which constituted 62.5% of the total vessels measured, aligning with the Swedish CArdioPulmonary BioImage Study cohort's[33] findings that the LAD had the highest prevalence of disease. However, we also found IMR-positive results in 32 LCx and 49 RCA, indicating that CMD can affect vessels beyond the left anterior descending artery.

Furthermore, the inconsistencies in IMR measurements in multiple coronary vessels indicated heterogeneity in microvascular function across different myocardial territories, potentially due to factors like blood flow characteristics, vessel dimensions, the supplied myocardial mass, and other mechanisms that remain to be elucidated[24,34]. IMR_{CT} overcomes this limitation by simultaneously assessing myocardial perfusion across all major coronary arteries, providing a practical solution for this issue.

Limitations

This study has several limitations. First, as a retrospective, single-centre study focusing on stable CAD patients, our analysis may be subject to selection bias. The current study also lacks standardised documentation of Canadian Cardiovascular Society class and New York Heart Association Functional Class, which limits our ability to correlate symptom severity with IMR_{CT} values. These gaps are being addressed in an ongoing multicentre prospective trial that is incorporating structured symptom assessment and hard clinical endpoints to fully define the clinical utility of IMR_{CT}. Second, inherent limitations of CCTA include reduced accuracy in patients with arrhythmias, tachycardia, or extensive coronary calcification – challenges that may be mitigated by future technical advancements and imaging strategies. Third, while IMR_{CT} reliably assesses hyperaemic microvascular resistance, it has inherent limitations in fully characterising CMD. Specifically, it cannot assess functional CMD manifestations or detect vasospastic components – since acetylcholine provocation testing was not performed – and requires complementary flow-based metrics such as CFR for a comprehensive evaluation. Emerging approaches like microvascular resistance reserve[35] may offer additional insights, particularly in patients with mixed disease phenotypes. However, current invasive protocols that integrate IMR, CFR, and vasomotor function testing remain the reference standard for a complete physiological assessment of the coronary microcirculation. Fourth, IMR_{CT} computation remains influenced by the accuracy of the outlet hyperaemic flow boundary conditions, and further efforts are needed to improve outlet flow estimation[36]. The vessel wall material parameters are currently based on fixed values derived from healthy subjects and are not personalised for individual patients, which may limit the accuracy of modelling vessel elasticity in specific cases. Additionally, the empirical relationship used to convert resting flow to hyperaemic flow is derived from population-level data and may not be fully applicable to all patient subgroups.

Conclusions

This study clarified the potential of IMR_{CT} measurements for CMD. Advancements in image reconstruction can improve the spatial resolution of CCTA and enhance the accuracy of IMR_{CT}, thereby facilitating early detection, precise assessment, and management of CMD.

Authors' affiliations

1. Department of Cardiovascular Medicine, Center for Circadian Metabolism and Cardiovascular Disease, Southwest Hospital, Army Medical University, Chongqing, China; 2. Key Laboratory of Geriatric Cardiovascular and Cerebrovascular Disease, Ministry of Education, Chongqing, China; 3. School of Biomedical Engineering, Sun Yat-sen University, Shenzhen, China; 4. Department of Radiology, Southwest Hospital, Army Medical University, Chongqing, China; 5. Department of Health Statistics, Army Medical University, Chongqing, China; 6. Archimedes Unit, Athena Research Centre, Athens, Greece; 7. Computer Science and Electronic Engineering, University of Essex, Colchester, United Kingdom; 8. Department of Medicine and Therapeutics, Faculty of Medicine, The Chinese University of Hong Kong, Hong Kong, China; 9. Bioengineering Department and Imperial-X, Imperial College London, London, United Kingdom

Funding

This study was supported by the Chongqing Talent Program (CQYC20210303360), the Chongqing Technological Innovation and Application Development Special Key Project (CSTB2023TIAD-KPX0061-2, CSTB2023TIAD-KPX0061-6), the National Natural Science Foundation of China (62101610, 62271511, 62101606, 62276282), the Chongqing Graduate Scientific Research and Innovation Project (CYB240291), and the Clinical Research Incubation Program of the First Affiliated Hospital of Army Medical University (2023IITZD04).

Conflict of interest statement

The authors have no conflicts of interest to declare.

References

1. Yang Z, Liu Y, Li Z, Feng S, Lin S, Ge Z, Fan Y, Wang Y, Wang X, Mao J. Coronary microvascular dysfunction and cardiovascular disease: Pathogenesis, associations and treatment strategies. *Biomed Pharmacother.* 2023;164:115011.

2. Likoff W, Segal BL, Kasparian H. Paradox of normal selective coronary arteriograms in patients considered to have unmistakable coronary heart disease. *N Engl J Med.* 1967;276:1063-6.

3. Vandeloo B, Andreini D, Brouwers S, Mizukami T, Monizzi G, Lochy S, Mileva N, Argacha JF, De Boulle M, Muyldermans P, Belmonte M, Sonck J, Gallinoro E, Munhoz D, Roosens B, Trabattoni D, Galli S, Seki R, Penicka M, Wyffels E, Mushtaq S, Nagumo S, Pardaens S, Barbato E, Bartorelli AL, De Bruyne B, Cosyns B, Collet C. Diagnostic performance of exercise stress tests for detection of epicardial and microvascular coronary artery disease: the UZ Clear study. *EuroIntervention.* 2023;18:e1090-8.

4. Bergamaschi L, De Vita A, Villano A, Tremamunno S, Armillotta M, Angeli F, Belmonte M, Paolisso P, Foà A, Gallinoro E, Polimeni A, Sucato V, Morrone D, Tuttolomondo D, Pavon AG, Guglielmo M, Gaibazzi N,

Mushtaq S, Perrone Filardi P, Indolfi C, Picano E, Pontone G, Lanza GA, Pizzi C; Coronary Physiopathology and Microcirculation Working Group of the Italian Society of Cardiology (SIC). Non-invasive imaging assessment in angina with non-obstructive coronary arteries (ANOCA). *Curr Probl Cardiol.* 2025;50:103021.

5. Schindler TH, Dilsizian V. Coronary Microvascular Dysfunction: Clinical Considerations and Noninvasive Diagnosis. *JACC Cardiovasc Imaging.* 2020;13:140-55.

6. Fearon WF, Balsam LB, Farouque HM, Caffarelli AD, Robbins RC, Fitzgerald PJ, Yock PG, Yeung AC. Novel index for invasively assessing the coronary microcirculation. *Circulation.* 2003;107:3129-32.

7. Fearon WF, Low AF, Yong AS, McGeoch R, Berry C, Shah MG, Ho MY, Kim HS, Loh JP, Oldroyd KG. Prognostic value of the Index of Microcirculatory Resistance measured after primary percutaneous coronary intervention. *Circulation.* 2013;127:2436-41.

8. Knuuti J, Wijns W, Saraste A, Capodanno D, Barbato E, Funck-Brentano C, Prescott E, Storey RF, Deaton C, Cuisset T, Agewall S, Dickstein K, Edvardsen T, Escaned J, Gersh BJ, Svitil P, Gilard M, Hasdai D, Hatala R, Mahfoud F, Masip J, Muneretto C, Valgimigli M, Achenbach S, Bax JJ; ESC Scientific Document Group. 2019 ESC Guidelines for the diagnosis and management of chronic coronary syndromes. *Eur Heart J.* 2020;41:407-77.

9. Collet C, Sakai K, Mizukami T, Ohashi H, Bouisset F, Caglioni S, van Hoe L, Gallinoro E, Bertolone DT, Pardaens S, Brouwers S, Storozhenko T, Seki R, Munhoz D, Tajima A, Buytaert D, Vanderheyden M, Wyffels E, Bartunek J, Sonck J, De Bruyne B. Vascular Remodeling in Coronary Microvascular Dysfunction. *JACC Cardiovasc Imaging.* 2024;17:1463-76.

10. Geng Y, Liu H, Wang X, Zhang J, Gong Y, Zheng D, Jiang J, Xia L. Effect of microcirculatory dysfunction on coronary hemodynamics: A pilot study based on computational fluid dynamics simulation. *Comput Biol Med.* 2022;146:105583.

11. Rabbat MG. Transforming the Coronary Artery Disease Care Pathway Bridging Computational Fluid Dynamics to Coronary CTA. *JACC Cardiovasc Imaging.* 2022;15:1059-62.

12. Yan Q, Xiao D, Jia Y, Ai D, Fan J, Song H, Xu C, Wang Y, Yang J. A multi-dimensional CFD framework for fast patient-specific fractional flow reserve prediction. *Comput Biol Med.* 2024;168:107718.

13. Narula J, Chandrashekhar Y, Ahmadi A, Abbara S, Berman DS, Blankstein R, Leipsic J, Newby D, Nicol ED, Nieman K, Shaw L, Villines TC, Williams M, Hecht HS. SCCT 2021 Expert Consensus Document on Coronary Computed Tomographic Angiography: A Report of the Society of Cardiovascular Computed Tomography. *J Cardiovasc Comput Tomogr.* 2021;15:192-217.

14. Kobayashi Y, Fearon WF. Invasive coronary microcirculation assessment--current status of index of microcirculatory resistance. *Circ J.* 2014;78:1021-8.

15. Kunadian V, Chieffo A, Camici PG, Berry C, Escaned J, Maas AHEM, Prescott E, Karam N, Appelman Y, Fraccaro C, Buchanan GL, Manzo-Silberman S, Al-Lamee R, Regar E, Lansky A, Abbott JD, Badimon L, Duncker DJ, Mehran R, Capodanno D, Baumbach A. An EAPCI Expert Consensus Document on Ischaemia with Non-Obstructive Coronary Arteries in Collaboration with European Society of Cardiology Working Group on Coronary Pathophysiology & Microcirculation Endorsed by Coronary Vasomotor Disorders International Study Group. *EuroIntervention.* 2021;16:1049-69.

16. Yong AS, Layland J, Fearon WF, Ho M, Shah MG, Daniels D, Whitbourn R, Macisaac A, Kritharides L, Wilson A, Ng MK. Calculation of the index of microcirculatory resistance without coronary wedge pressure measurement in the presence of epicardial stenosis. *JACC Cardiovasc Interv.* 2013;6:53-8.

17. Xue X, Deng D, Zhang H, Gao Z, Zhu P, Hau WK, Zhang Z, Liu X. Non-Invasive Assessment of Coronary Microvascular Dysfunction Using Vascular Deformation-Based Flow Estimation. *IEEE Trans Biomed Eng.* 2024;71:3000-13.

18. Gao Z, Wang X, Sun S, Wu D, Bai J, Yin Y, Liu X, Zhang H, de Albuquerque VHC. Learning physical properties in complex visual scenes: An intelligent machine for perceiving blood flow dynamics from static CT angiography imaging. *Neural Netw.* 2020;123:82-93.

19. Tu S, Westra J, Yang J, von Birgelen C, Ferrara A, Pellicano M, Nef H, Tebaldi M, Murasato Y, Lansky A, Barbato E, van der Heijden LC, Reiber JHC, Holm NR, Wijns W; FAVOR Pilot Trial Study Group. Diagnostic Accuracy of Fast Computational Approaches to Derive Fractional Flow Reserve From Diagnostic Coronary Angiography: The International Multicenter FAVOR Pilot Study. *JACC Cardiovasc Interv.* 2016;9:2024-35.

20. Pfaller MR, Pham J, Verma A, Pegolotti L, Wilson NM, Parker DW, Yang W, Marsden AL. Automated generation of 0D and 1D reduced-order models of patient-specific blood flow. *Int J Numer Method Biomed Eng.* 2022;38:e3639.

21. Xue X, Liu X, Gao Z, Wang R, Xu L, Ghista D, Zhang H. Personalized coronary blood flow model based on CT perfusion to non-invasively calculate fractional flow reserve. *Computer Methods in Applied Mechanics and Engineering.* 2023;404:115789.

22. Olufsen MS. Structured tree outflow condition for blood flow in larger systemic arteries. *Am J Physiol.* 1999;276:H257-68.

23. Li W, Takahashi T, Rios SA, Latib A, Lee JM, Fearon WF, Kobayashi Y. Diagnostic performance and prognostic impact of coronary angiography-based Index of Microcirculatory Resistance assessment: A systematic review and meta-analysis. *Catheter Cardiovasc Interv.* 2022;99:286-92.

24. Tamaru H, Fujii K, Fukunaga M, Imanaka T, Kawai K, Miki K, Horimatsu T, Nishimura M, Saita T, Sumiyoshi A, Shibuya M, Masuyama T, Ishihara M. Mechanisms of gradual pressure drop in angiographically normal left anterior descending and right coronary artery: Insights from wave intensity analysis. *J Cardiol.* 2021;78:72-8.

25. Kaski JC. Overview of gender aspects of cardiac syndrome X. *Cardiovasc Res.* 2002;53:620-6.

26. Li JJ, Zhu CG, Nan JL, Li J, Li ZC, Zeng HS, Gao Z, Qin XW, Zhang CY. Elevated circulating inflammatory markers in female patients with cardiac syndrome X. *Cytokine.* 2007;40:172-6.

27. Jones S, McNeil M, Koczo A. Updates in Cardiovascular Disease Prevention, Diagnosis, and Treatment in Women. *Med Clin North Am.* 2023;107:285-98.

28. Aribas E, Roeters van Lennep JE, Elias-Smale SE, Piek JJ, Roos M, Ahmadizar F, Arshi B, Duncker DJ, Appelman Y, Kavousi M. Prevalence of microvascular angina among patients with stable symptoms in the absence of obstructive coronary artery disease: a systematic review. *Cardiovasc Res.* 2022;118:763-71.

29. Mileva N, Nagumo S, Mizukami T, Sonck J, Berry C, Gallinoro E, Monizzi G, Candreva A, Munhoz D, Vassilev D, Penicka M, Barbato E, De Bruyne B, Collet C. Prevalence of Coronary Microvascular Disease and Coronary Vasospasm in Patients With Nonobstructive Coronary Artery Disease: Systematic Review and Meta-Analysis. *J Am Heart Assoc.* 2022;11:e023207.

30. Ford TJ, Stanley B, Good R, Rocchiccioli P, McEntegart M, Watkins S, Eteiba H, Shaukat A, Lindsay M, Robertson K, Hood S, McGeoch R, McDade R, Yii E, Sidik N, McCartney P, Corcoran D, Collison D, Rush C, McConnachie A, Touyz RM, Oldroyd KG, Berry C. Stratified Medical Therapy Using Invasive Coronary Function Testing in Angina: The CorMicA Trial. *J Am Coll Cardiol.* 2018;72:2841-55.

31. Lee JM, Koo BK, Shin ES, Nam CW, Doh JH, Hwang D, Park J, Kim KJ, Zhang J, Hu X, Wang J, Ahn C, Ye F, Chen S, Yang J, Chen J, Tanaka N, Yokoi H, Matsuo H, Takashima H, Shiono Y, Akasaka T. Clinical implications of three-vessel fractional flow reserve measurement in patients with coronary artery disease. *Eur Heart J.* 2018;39:945-51.

32. Kobayashi Y, Lee JM, Fearon WF, Lee JH, Nishi T, Choi DH, Zimmermann FM, Jung JH, Lee HJ, Doh JH, Nam CW, Shin ES, Koo BK. Three-Vessel Assessment of Coronary Microvascular Dysfunction in Patients With Clinical Suspicion of Ischemia: Prospective Observational Study With the Index of Microcirculatory Resistance. *Circ Cardiovasc Interv.* 2017;10:e005445.

33. Bergström G, Persson M, Adiels M, Björnson E, Bonander C, Ahlström H, Alfredsson J, Angerås O, Berglund G, Blomberg A, Brandberg J, Börjesson M, Cederlund K, de Faire U, Duvernoy O, Ekblom Ö, Engström G, Engvall JE, Fagman E, Eriksson M, Erlinge D, Fagerberg B, Flinck A, Gonçalves I, Hagström E, Hjelmgren O, Lind L, Lindberg E, Lindqvist P, Ljungberg J, Magnusson M, Mannila M, Markstad H, Mohammad MA, Nystrom FH, Ostenfeld E, Persson A, Rosengren A,

Sandström A, Själander A, Sköld MC, Sundström J, Swahn E, Söderberg S, Torén K, Östgren CJ, Jernberg T. Prevalence of Subclinical Coronary Artery Atherosclerosis in the General Population. *Circulation*. 2021;144:916-29.

34. Muroya T, Kawano H, Yamamoto F, Maemura K. Coronary microvascular resistance comparison of coronary arteries with and without considering vascular diameter: A retrospective, single-center study. *Health Sci Rep*. 2023;6:e1714.

35. Gallinoro E, Bertolone DT, Mizukami T, Paolisso P, Bermpeis K, Munhoz D, Sakai K, Seki R, Ohashi H, Esposito G, Caglioni S, Mileva N, Leone A, Candreva A, Belmonte M, Storozhenko T, Viscusi MM, Vanderheyden M, Wyffels E, Bartunek J, Sonck J, Barbato E, Collet C, De Bruyne B. Continuous vs Bolus Thermodilution to Assess Microvascular Resistance Reserve. *JACC Cardiovasc Interv*. 2023;16:2767-77.

36. Lodi Rizzini M, Candreva A, Chiastra C, Gallinoro E, Calò K, D'Ascenzo F, De Bruyne B, Mizukami T, Collet C, Gallo D, Morbiducci U. Modelling coronary flows: impact of differently measured inflow boundary conditions on vessel-specific computational hemodynamic profiles. *Comput Methods Programs Biomed*. 2022;221:106882.

Supplementary data

Supplementary Appendix 1. Methodology of IMR_{CT} computation.
Supplementary Table 1. Consistency analysis of vessel counts and intervascular IMR values in patient measurements.
Supplementary Table 2. Functional phenotyping of coronary physiology in the study population.
Supplementary Table 3. Number of vessels with IMR_{CT} and IMR above and below the threshold value of 25.
Supplementary Table 4. Number of vessels with IMR_{CT} and IMR above or below 25 grouped by sex, hypertension, and diabetes status.
Supplementary Table 5. Diagnostic efficacy of IMR_{CT} for IMR ≥25 categorised by sex, hypertension, and diabetes status at the vessel level.
Supplementary Table 6. Number of vessels with IMR_{CT} and IMR above or below 25 grouped by location: LAD, LCx, and RCA.
Supplementary Table 7. Diagnostic efficacy of IMR_{CT} at the vessel level for IMR ≥25 in the LAD, LCx, and RCA.
Supplementary Figure 1. Simplified schematic of the IMR_{CT} computational pipeline.
Supplementary Figure 2. Workflow diagram of the IMR_{CT} model.
Supplementary Figure 3. Study flowchart.
Supplementary Figure 4. Examples of IMR_{CT} computations for case 42, wherein all three coronary vessels exhibited concordant IMR values.
Supplementary Figure 5. Examples of IMR_{CT} computations for case 128, wherein all three coronary vessels exhibited discordant IMR values.
Supplementary Figure 6. Passing-Bablok regression analysis between IMR_{CT} and invasive IMR measurements.
Supplementary Figure 7. Examples of IMR_{CT} computation under different physiological scenarios.
Supplementary Figure 8. Decision curve analysis of the IMR_{CT}-based predictive model.

The supplementary data are published online at: https://eurointervention.pcronline.com/doi/10.4244/EIJ-D-25-00671

Supplementary data

Supplementary Appendix 1. Methodology of IMR_{CT} computation.

1. Overview of the IMR_{CT} model

We propose a model designed to noninvasively compute the index of microcirculatory resistance (IMR) from coronary computed tomography angiography (CCTA), a promising technique for quantitatively assessing coronary microvascular dysfunction (CMD). The model directly estimates hyperemic coronary blood flow (CBF), which serves as the essential input for IMR_{CT} computation. A simplified schematic of the overall computational pipeline is presented in **Supplementary Figure 1**, highlighting the modular workflow from CCTA image processing to final IMR_{CT} output. A more detailed diagram of the modeling strategy is provided in **Supplementary Figure 2**, outlining the major computational steps, including vascular deformation extraction, CBF estimation through inverse modeling, and computational fluid dynamics (CFD) simulation. Briefly, the model extracts vascular deformations from multi-phase CCTA and applies inverse problem-solving to estimate hyperemic CBF based on physical constraints between deformation and flow. This approach allows for individualized estimation of CBF by ensuring the appropriate application of constraints on vascular deformation in each segment. The estimated CBF is then used to define outlet boundary conditions for patient-specific CFD simulation, from which pressure and velocity fields are computed to derive IMR_{CT}. The total computation time is divided into three components: coronary segmentation and vascular deformation extraction (approximately 5 minutes), CBF estimation (approximately 5 minutes), and three-dimensional (3D) CFD simulation (approximately 20 minutes).

2. Inverse problem solving of CBF

2.1 Coronary segmentation

The algorithm for coronary lumen segmentation is from our previous study[18]. First, this segmentation method locates the aorta by detecting a circle-like object in CCTA images via Hough transform. After that, it detects the location of the intersection between the aorta and the coronary artery (i.e. the root of coronary tree) by the region growing strategy. The location of the coronary root is considered within a circular region. The diameter of the circular region is 1.2 times larger than the radius of the aorta. Second, the image patch is obtained by using a 3D window centered as the coronary root. Within this image patch, we apply U-net for detecting the region of the coronary artery and the dynamic programming algorithm for extracting the segment of the coronary centerline. Finally, a 3D window is moved along the

direction of the detected centerline segment. The above detection procedure of coronary region and centerline is repeated until the entire coronary artery is segmented. We employ the above steps on multi-phase CCTA images to segment the coronary artery models at different phases. In addition, a standard truncation strategy is applied at the outlet of the first-generation branch of the main 3D coronary artery model, approximately five times the diameter from the bifurcation[21]. This method can reduce the impact of spatial resolution limitations of CCTA, thereby enhancing the coronary segmentation reliability.

2.2 Vascular deformation extraction and constraint sampling

After coronary segmentation, we extract vascular deformation by analyzing the dynamic changes in lumen dimensions throughout the cardiac cycle. We calculate the cross-sectional area at various points along the coronary centerline, focusing on changes in the lumen. For coronary CCTA images acquired at different phases, we extract and align the centerline across each phase using non-rigid registration techniques, with vascular bifurcation points serving as key landmarks. This alignment ensures accurate tracking of lumen changes at each point across different time phases. To ensure accuracy, we limit the analysis to vessels with diameters greater than 2 mm, as smaller vessels are more prone to measurement errors. We also implement an error control mechanism, applying smoothing and data fitting techniques to reduce noise and improve data reliability. This approach provides robust analysis of vessel deformation, which is crucial for accurate coronary flow assessment.

This study acquires CCTA images using retrospective ECG gating and reconstructs the entire cardiac cycle into 10 evenly spaced phases. For a typical heart rate range of 60-75 beats per minute, this protocol provides a temporal resolution of approximately 80-100 milliseconds per phase. The IMR_{CT} simulation requires the average blood flow as a boundary condition; therefore, this method aims to estimate the average blood flow over the cardiac cycle. In this approach, the amplitude of vessel deformation (i.e., the range between maximum and minimum cross-sectional area) serves as the primary feature. This metric is expected to reflect average flow while being relatively insensitive to instantaneous deformation details. Given this consideration, a sampling density of 10 phases is considered adequate to capture the essential deformation dynamics required for accurate flow estimation.

Regarding the sampling interval and number of cross-sectional constraints for vascular deformation, we extract deformation data from multi-phase CCTA by sampling cross-sectional areas along the coronary artery centerline at regular intervals of approximately 2-3 mm. Since the major coronary arteries and their branches typically extend over several centimeters to about 10 cm, this approach yields dozens of cross sections per vessel segment. This spatial

resolution effectively captures the spatial distribution of vascular deformation and enables robust inverse modeling. Moreover, the sampling density meets the constraint requirements of inverse modeling and supports stable and reliable estimation of CBF.

To ensure modeling accuracy while considering the limitations of image resolution, vascular deformation and cross-sectional area constraints are applied only to vessel segments with diameters greater than 2 mm. Given the spatial resolution of coronary CTA (~0.3 mm), the corresponding cross-sectional area includes about 40-140 pixels, which is sufficient for quantifying area changes and applying physical constraints in inverse modeling. In contrast, for vessel segments with diameters smaller than 2 mm, direct cross-sectional analysis is not performed due to increased susceptibility to imaging artifacts and segmentation inaccuracies. Instead, blood flow in these small segments is inferred based on the principle of mass conservation and the estimated flow in adjacent, larger vessel segments. This approach enables CBF estimation across the entire coronary artery tree, facilitating IMR_{CT} computation.

2.3 Inverse estimation of resting coronary flow

The concept of inverse problem solving provides the possibility to estimate CBF based on vascular deformation extracted from multi-phase CCTA. Solving an inverse problem requires establishing a physical relationship between known variables and the unknown solution variable. Vascular deformation is influenced by blood flow. Therefore, we can estimate blood flow by inversely solving for temporal deformation in the vascular cross-sectional area from multi-phase CCTA. Here, we assume the vessel wall is impermeable and the blood is an incompressible Newtonian fluid. Vascular deformation refers to changes in cross-sectional area. The centerline at the 0% cardiac phase is used as the baseline model for inverse problem solving. The hydrodynamic equations can express the physical relationship between vascular deformation and blood flow:

$$\frac{\partial Q}{\partial t} + \frac{4}{3}\frac{\partial}{z}\left(\frac{Q^2}{S}\right) + \frac{S}{\rho}\frac{\partial p}{\partial z} = Sf - N\frac{Q}{S} + \frac{\mu}{\rho}\frac{\partial^2 Q}{\partial z^2} \quad (1)$$

$$\frac{\partial S}{\partial t} + \frac{\partial Q}{\partial z} = 0 \quad (2)$$

$$P(z,t) = P^0(z) + \frac{4}{3}\left(k_1 e^{k_2 r^0(z)} + k_3\right)\left(1 - \sqrt{\frac{S^0(z)}{S(z,t)}}\right) \quad (3)$$

where z is the blood vessel's centerline axial coordinate; Q is the flow rate; p is the pressure; t is the time; S is the cross-sectional area; ρ is the density of blood; f is the body force; P^0 is the reference pressure; r0 is the reference radius; k1, k2, and k3 are material properties of elastic wall. We employ a nonlinear (Olufsen) constitutive material model in this study, with $k_1 = 2.00 \times 10^7$ g·s^{-2}·cm^{-1}, $k_2 = -22.53$ cm^{-1}, and $k_3 = 8.65 \times 10^5$ g·s^{-2}·cm^{-1}. The choice of velocity profile

determines the variable N[20]. These three mathematical equations describe the relationship between vascular deformation, CBF, and blood pressure. For the coronary artery model, the blood pressure at the coronary artery inlet and the vascular deformation across the entire coronary artery can be considered as known variables, while CBF is the unknown variable. We can apply the concept of solving inverse problems to implicitly derive the CBF. Specifically, we adjust the parameters of the lumpted parameter model to fit both the vascular deformation and blood pressure, thereby obtaining the target CBF, as shown in **Supplementary Figure 2B**. The numerical solution of this inverse problem for estimating CBF can utilize the zero-dimensional lumped parameter model as a boundary condition[17], as illustrated in **Supplementary Figure 2**. The coronary inlet pressure curve is regulated by adjusting the parameters within the heart, aorta, systemic circulation, and pulmonary modules. This curve can be calibrated using cuff-measured blood pressure prior to CCTA. By optimizing the lumped parameter model parameters, the simulation results align with the clinical observation data (vascular deformation and brachial cuff pressure), ultimately yielding the resting CBF. This approach avoids circular reasoning because the parameter adjustment does not rely on fitting the blood flow curve to reverse-predict blood flow; instead, it predicts blood flow by fitting vascular deformation and pressure data.

Using this method, we can determine the CBF for each vascular segment, including the total at the inlet and the flow at each outlet. Vascular segments are delineated based on the locations of coronary bifurcations. In cases of parameter discrepancies, the simulated annealing algorithm is employed to optimize these parameters. The least-squares error E quantifies the discrepancies between the vascular deformation and coronary inlet pressure relative to the ground truth, and is defined as follows:

$$E^{A} = \sum_{n=1}^{N}(A_{cal}^{n} - A_{GT}^{n})^{2} \quad (4)$$

$$E^{P} = \sum_{k=1}^{K}(P_{cal}^{k} - P_{GT}^{k})^{2} \quad (5)$$

In this analysis, E^{A} represents the errors between the vascular deformation curve and the ground truth, while E^{P} denotes the errors between the coronary inlet pressure and the ground truth. The variables n and k correspond to the sampling points on the vascular deformation and coronary inlet pressure, respectively. Furthermore, A_{cal}^{n} and P_{cal}^{k} indicate the calculated cross-sectional area and coronary inlet pressure, with A_{GT}^{n} and P_{GT}^{k} representing the respective ground truths.

It is important to note that the precision of vascular deformation extraction varies across different vascular segments due to the spatial resolution limitations of CCTA. The imaging

quality of CCTA improves as the diameter of the vessels increases, resulting in the highest reliability in extracting vascular deformation in larger vessel segments. Therefore, to enhance the estimation of CBF, it is necessary to assign differential error weights, E, to various vascular segments. The coronary inlet vascular segment, which has the largest diameter, requires the highest error weights. This segment's blood flow reflects the total CBF across all downstream coronary segments, and the accuracy of this measurement is critical for determining the distribution of outlet blood flow. Moderate error weights are assigned to the main branch vascular segments, while smaller branch vessels receive lower weights. The total E is the cumulative sum of errors at all observation positions:

$$E_{total} = \sum_{j=1}^{J} w_h \, E_j^A + E^P \quad (6)$$

In this model, w_h represents the differential error weights assigned to each vascular segment, E_j^A quantifies the vascular deformation error at various observation positions compared to the ground truth, and j denotes these observation positions. Additionally, E^P represents the errors in the coronary inlet pressure relative to the ground truth.

2.4 Hyperemic flow estimation

Previous research has demonstrated that the relationship between hyperemic CBF and resting CBF follows a quadratic function[19]. This relationship was established based on population-level data without explicit subgroup stratification, and is intended to provide a generally applicable estimation of hyperemic flow across patient populations. Using this function, we can adjust the total resting CBF to reflect maximal hyperemia. The total hyperemic CBF (Q_{total}^{hyp}) is expressed as follows:

$$Q_{total}^{hyp} = c_0 + c_1 \times Q_{total}^{rest} + c_2 \times (Q_{total}^{rest})^2 \quad (7)$$

where c_0, c_1, and c_2 are 0.10, 1.55 and -0.93. We allocate the total hyperemic CBF $Q_{out,i}^{hyp}$ at each outlet based on the proportional distribution of resting CBF, which is described as follows:

$$Q_{out,i}^{hyp} = Q_{total}^{hyp} \times \frac{Q_{out,i}^{rest}}{Q_{total}^{rest}} \quad (8)$$

where $Q_{out,i}^{hyp}$ and Q_{total}^{hyp} are mean blood flow.

2.5 Vessel wall material parameters

In this study, the material parameters k_1, k_2, and k_3 are adopted from the nonlinear elastic vessel wall model proposed by Olufsen et al.[22], with values of $k_1 = 2.00 \times 10^7$ g·s^{-2}·cm^{-1}, $k_2 = -22.53$ cm^{-1}, and $k_3 = 8.65 \times 10^5$ g·s^{-2}·cm^{-1}. These constants are empirically derived from vessel compliance data of healthy subjects and represent the average elastic properties of normal

arteries. In our model, these parameters are applied as fixed constants to all patients' normal vessel segments and do not incorporate patient-specific variations. We acknowledge this as a limitation of the current model, as patient-specific personalization of vessel elasticity in normal segments is not implemented.

2.6 Handling of calcified segments

Our method is applicable to patients with calcified lesions. In these cases, we adopt a selective constraint strategy to ensure modeling accuracy. Specifically, vascular deformation constraints are applied only to anatomically normal and elastically preserved vessel segments, while calcified plaque regions are explicitly excluded from such constraints. This selective approach prevents potential errors caused by insufficient deformation in calcified areas, while in the non-calcified regions, the vessels retain good elasticity, allowing for significant deformation and a more accurate reflection of dynamic blood flow changes. Moreover, we leverage the principle of flow conservation between vessel segments. Since blood flow in the coronary system is continuous, even if certain segments are not constrained due to calcification, their blood flow is still influenced by other normal vessel segments. Therefore, despite minimal deformation in calcified regions, we can accurately infer the blood flow in these areas using deformation data from upstream and downstream non-calcified segments, effectively compensating for the impact of insufficient deformation. Additionally, the coronary inlet segment typically experiences less calcification, and deformation in this segment is directly related to the total blood flow. As this segment reflects the total blood flow of all downstream coronary segments, deformation constraints applied here are critical for estimating overall blood flow. By assigning higher error weights and applying deformation constraints to these key inlet segments, we ensure accurate blood flow estimation, which is propagated to calcified regions through flow conservation. Ultimately, this strategy allows for the estimation of the CBF at the outlet ($Q_{out,i}^{rest}$). The blood flow at the inlet vascular segment constitutes the total CBF (Q_{total}^{rest}), where both $Q_{out,i}^{rest}$ and Q_{total}^{rest} represent average blood flow rates.

3. IMR_{CT} computation

3.1 Mesh generation

The IMR_{CT} computation process includes reconstructing the coronary 3D model, generating meshes, setting boundary conditions, and performing steady-state 3D CFD simulations, as illustrated in **Supplementary Figure 2**. To minimize computation time and cost, we focus solely on the target vessel's IMR_{CT} in this study. A high-quality tetrahedral mesh is generated for the selected model. Based on our prior mesh sensitivity analysis, a refined mesh with approximately one million elements is sufficient for accurate CFD simulations of the coronary

artery model[21].

3.2 Boundary condition

During clinical IMR assessments, the coronary inlet pressure is typically equated to the mean aortic pressure (MAP). It is assumed that the difference between the MAP in the resting state and during hyperemia is negligible. Consequently, the steady-state inlet boundary condition (BC_{inlet}) can be expressed as follows:

$$\mathrm{BC_{inlet}} = \mathrm{MAP} = 0.4 \times (\mathrm{SBP} - \mathrm{DBP}) + \mathrm{DBP} \quad (9)$$

In this model, SBP and DBP denote the brachial systolic and diastolic blood pressures, respectively. The IMR_{CT} computation uses the mean outlet blood flow as the outlet boundary condition. The steady-state boundary conditions at the ith outlet are formulated as follows:

$$\mathrm{BC_{outlet}} = \mathrm{Q_{out,i}^{hyp}} \quad (10)$$

where $\mathrm{Q_{out,i}^{hyp}}$ is the mean outlet CBF at hyperemia stat.

3.3 3D CFD simulation

To simulate the hemodynamics of patient-specific coronary arteries, we solve the incompressible Newtonian Navier-Stokes equations to calculate flow velocity and pressure distribution within the coronary artery. The CFD simulation in this study is conducted under steady-state flow conditions. This modeling choice aligns with the invasive IMR measurement. IMR is defined as the product of distal coronary pressure (Pd) and the mean transit time (Tmn) of blood flow. Specifically, Pd represents the average pressure over several cardiac cycles rather than an instantaneous pressure waveform. Tmn refers to the average time required for saline to travel from the coronary ostium to the distal measurement site, reflecting the overall behavior of blood flow over time instead of capturing instantaneous fluctuations in flow velocity. Given that both Pd and Tmn are time-averaged parameters, using steady-state CFD for IMR_{CT} computation is a consistent and appropriate modeling choice. These equations are defined as follows:

$$\frac{\partial \vec{u}}{\partial t} + (\vec{u} \cdot \nabla)\vec{u} = -\frac{1}{\rho}\nabla p + \nu\nabla^2\vec{u} \quad (11)$$

$$\nabla \cdot \vec{u} = 0 \quad (12)$$

In this model, u and p represent the velocity and pressure, respectively, while v and ρ denote the viscosity and density of blood, set at 0.0035 Pa•s and 1050 kg/m^3, respectively. Blood is considered an isotropic, uniform, and incompressible Newtonian fluid, with blood flow in the vessel lumen idealized as laminar. We also assume that the vessel wall is rigid and adheres to a non-slip condition. Following the CFD simulation, the IMR_{CT} is calculated as follows:

$$IMR_{CT} = Pd \times Tmn \quad (13)$$

where Pd is the mean distal pressure, Tmn is the mean transit time.

The CFD simulation in this study uses coronary geometry extracted from the 70% phase of the cardiac cycle, which corresponds to mid-to-late diastole. CBF predominantly occurs during diastole, as myocardial compression during systole significantly reduces coronary perfusion. Therefore, employing coronary geometry from the diastolic phase more accurately reflects the vessel configuration during the period of active coronary flow, thereby enhancing the physiological relevance of IMR_{CT} computation.

After the CFD simulation, Tmn is computed through a segment-wise accumulation of local transit times along the vessel centerline. For each vessel segment, the local transit time is calculated as the ratio of segment volume to flow rate, and the total Tmn is expressed as:

$$Tmn = \sum_{i=1}^{n} T_i = \sum_{i=1}^{n} \frac{V_i}{Q_i} \quad (14)$$

where V_i is the volume of segment $_i$, and Q_i is the corresponding flow rate obtained from steady-state CFD simulation. This formulation is consistent with the theoretical definition of clinically measured Tmn, which reflects the mean time required for blood to traverse a vessel segment. It is also consistent with our previously published framework[17], where the same method is validated against invasive clinical measurements.

The IMR_{CT} computation pipeline in this study is implemented based on automated algorithms, covering key steps including coronary segmentation and 3D reconstruction, vascular deformation extraction, blood flow estimation, boundary condition setting, CFD simulation, and IMR_{CT} calculation. The workflow is designed to minimize operator-related variability and enhance consistency and reproducibility of the computation.

4. Validation of resting CBF

We can use the Tmn as a reliable indicator to verify CBF. The clinical invasive measurement of IMR requires the use of a temperature/pressure wire to obtain the thermodilution curve under maximal hyperemia. According to the thermodilution principle, the Tmn of room temperature saline injected into the coronary artery is inversely correlated with the blood flow velocity (F) measured by invasive methods. The formula for the thermodilution principle is as follows:

$$Tmn = V/F \quad (15)$$

where F is the CBF, V is the epicardial vascular volume between the injection site and the sensor, and Tmn is the mean transit time of the injected indicator. For a given vessel, V remains constant, so the inverse of the Tmn is directly proportional to the flow velocity.

Therefore, Tmn can serve as a proxy for blood flow. To validate the accuracy of the IMR_{CT} model, we can compare the Tmn calculated by the model with the clinically measured Tmn. This comparison allows us to evaluate the precision of the blood flow estimates produced by the model.

We have validated the IMR_{CT} model's blood flow estimation by comparing the Tmn between the model's calculations and invasive clinical measurements, using data from 216 blood vessels analyzed in this study. As shown in **Figure 2** of the main text, the correlation coefficient between the Tmn calculated by the IMR_{CT} model and the invasive Tmn is 0.79, with agreement limits ranging from -0.57 to 0.68. These results demonstrate both high correlation and consistency, verifying the accuracy and reliability of the IMR_{CT} model's blood flow estimation.

Supplementary Table 1. Consistency analysis of vessel counts and intervascular IMR values in patient measurements.

Number of vessels measured in a patient	
1	141 (80.1)
2	30 (17.1)
3	5 (2.8)
Consistency of IMR values in multi-vessel IMR assessments -	
Concordance for IMR ≥ 25 or <25	20 (57.1)
Discordance	15 (42.9)

The values are presented as n (%).

IMR: index of microcirculatory resistance.

Supplementary Table 2. Functional phenotyping of coronary physiology in the study population.

Category	Overall (n=176)	Female (n=61)	Male (n=115)
FFR > 0.8	123 (69.9%)	48 (78.7%)	75 (65.2%)
Normal (CFR≥2.0, IMR<25)	65 (36.9%)	25 (41.0%)	40 (34.8%)
Isolated IMR elevation (CFR≥2.0, IMR≥25)	41 (23.3%)	16 (26.2%)	25 (21.7%)
Mixed Dysfunction (CFR<2.0, IMR≥25)	9 (5.1%)	5 (8.2%)	4 (3.5%)
Functional CMD (CFR<2.0, IMR<25)	8 (4.5%)	2 (3.3%)	6 (5.2%)
FFR ≤ 0.8	53 (30.1%)	13 (21.3%)	40 (34.8%)
IMR ≥ 25	15 (8.5%)	4 (6.6%)	11 (9.6%)
IMR < 25	38 (21.6%)	9 (14.8%)	29 (25.2%)
CFR < 2.0	27 (15.3%)	9 (14.8%)	18 (15.7%)

The values are presented as n (%).

CFR: coronary flow reserve; CMD: coronary microvascular dysfunction; FFR: fractional flow reserve; IMR: index of microcirculatory resistance.

Supplementary Table 3. Number of vessels with IMR_{CT} and IMR above and below the threshold value of 25.

	Per-vessel		Per-patient	
	IMR ≥ 25	IMR < 25	IMR ≥ 25	IMR < 25
IMR_{CT} ≥ 25	59	25	53	22
IMR_{CT} < 25	14	118	12	89

IMR: index of microcirculatory resistance; IMR_{CT}: coronary computed tomography angiography-based IMR

.

Supplementary Table 4. Number of vessels with IMR_{CT} and IMR above or below 25 grouped by sex, hypertension, and diabetes status.

	Female		Male		Hypertension		No hypertension		Diabetes		No diabetes	
	IMR ≥ 25	IMR < 25	IMR ≥ 25	IMR < 25	IMR ≥ 25	IMR < 25	IMR ≥ 25	IMR < 25	IMR ≥ 25	IMR < 25	IMR ≥ 25	IMR < 25
IMR_{CT} ≥ 25	34	17	25	8	48	19	11	6	34	11	25	14
IMR_{CT} < 25	9	62	5	56	10	84	4	34	10	57	4	61

IMR: index of microcirculatory resistance; IMR_{CT}: coronary computed tomography angiography-based IMR.

Supplementary Table 5. Diagnostic efficacy of IMR_{CT} for IMR ≥25 categorised by sex, hypertension, and diabetes status at the vessel level.

	No.	IMR ≥ 25 n (%)	Accuracy (%)	Sensitivity (%)	Specificity (%)	PPV (%)	NPV (%)	AUC
Female	122	43 (35.2%)	78.7 (70.2 to 92.3)	79.1 (64.0 to 90.0)	78.5 (67.8 to 87.0)	66.7 (56.1 to 75.8)	87.3 (79.2 to 92.6)	0.79 (0.70 to 0.86)
Male	94	30 (31.9%)	86.2 (77.5 to 92.4)	83.3 (65.3 to 94.4)	87.5 (76.8 to 94.4)	75.8 (61.6 to 85.9)	91.8 (83.3 to 96.2)	0.85 (0.77 to 0.92)
Hypertension	161	58 (36.0%)	82.0 (75.2 to 87.6)	82.8 (70.6 to 91.4)	81.6 (72.7 to 88.5)	71.6 (62.3 to 79.4)	89.4 (82.6 to 93.7)	0.82 (0.75 to 0.88)
No hypertension	55	15 (27.2%)	81.8 (69.1 to 90.9)	73.3 (44.9 to 92.2)	85.0 (70.2 to 94.3)	64.7 (45.2 to 80.3)	89.5 (78.4 to 95.2)	0.79 (0.66 to 0.89)
Diabetes	112	44 (39.3%)	81.3 (72.8 to 88.0)	77.3 (62.2 to 88.5)	83.8 (72.9 to 91.6)	75.6 (63.7 to 84.5)	85.1 (76.6 to 90.9)	0.81 (0.72 to 0.90)
No diabetes	104	29 (27.9%)	82.7 (74.0 to 89.4)	86.2 (68.3 to 96.1)	81.3 (70.7 to 89.4)	64.1 (52.1 to 74.5)	93.9 (85.9 to 97.4)	0.84 (0.75 to 0.90)

The values are presented as % (95% confidence interval).

AUC: area under the receiver operating characteristic curve; IMR: index of microcirculatory resistance; IMR_{CT}: coronary computed tomography angiography-based IMR; NPV: negative predictive value; PPV: positive predictive value.

Supplementary Table 6. Number of vessels with IMR_{CT} and IMR above or below 25 grouped by location: LAD, LCx, and RCA.

	LAD		LCX		RCA	
	IMR ≥ 25	IMR < 25	IMR ≥ 25	IMR < 25	IMR ≥ 25	IMR < 25
IMR_{CT} ≥ 25	30	21	8	1	21	3
IMR_{CT} < 25	7	77	4	19	3	22

IMR: index of microcirculatory resistance; IMR_{CT}: coronary computed tomography angiography-based IMR.LAD: left anterior descending artery; LCX: left circumflex artery; RCA: right coronary artery.

Supplementary Table 7. Diagnostic efficacy of IMR_{CT} at the vessel level for IMR ≥25 in the LAD, LCx, and RCA.

	No.	IMR ≥ 25 n (%)	Accuracy	Sensitivity	Specificity	PPV	NPV	AUC
LAD	135	37 (27.4%)	79.3 (71.4 to 85.8)	81.1 (64.8 to 92.0)	78.6 (64.8 to 92.0)	58.8 (48.7 to 68.3)	91.7 (84.9 to 95.6)	0.80 (0.72 to 0.86)
LCX	32	12 (37.5%)	84.4 (67.2 to 94.7)	66.7 (34.9 to 90.1)	95.0 (75.1 to 99.9)	88.9 (53.2 to 98.3)	82.6 (68.0 to 91.4)	0.81 (0.63 to 0.93)
RCA	49	24 (49.0%)	87.8 (75.2 to 95.4)	87.5 (67.7 to 97.3)	88.0 (68.8 to 97.5)	87.5 (70.6 to 95.3)	88.0 (71.6 to 95.5)	0.88 (0.75 to 0.95)

The values are presented as % (95% confidence interval).

IMR: index of microcirculatory resistance; IMR_{CT}: coronary computed tomography angiography-based IMR; LAD: left anterior descending artery; LCX: left circumflex artery; RCA: right coronary artery.

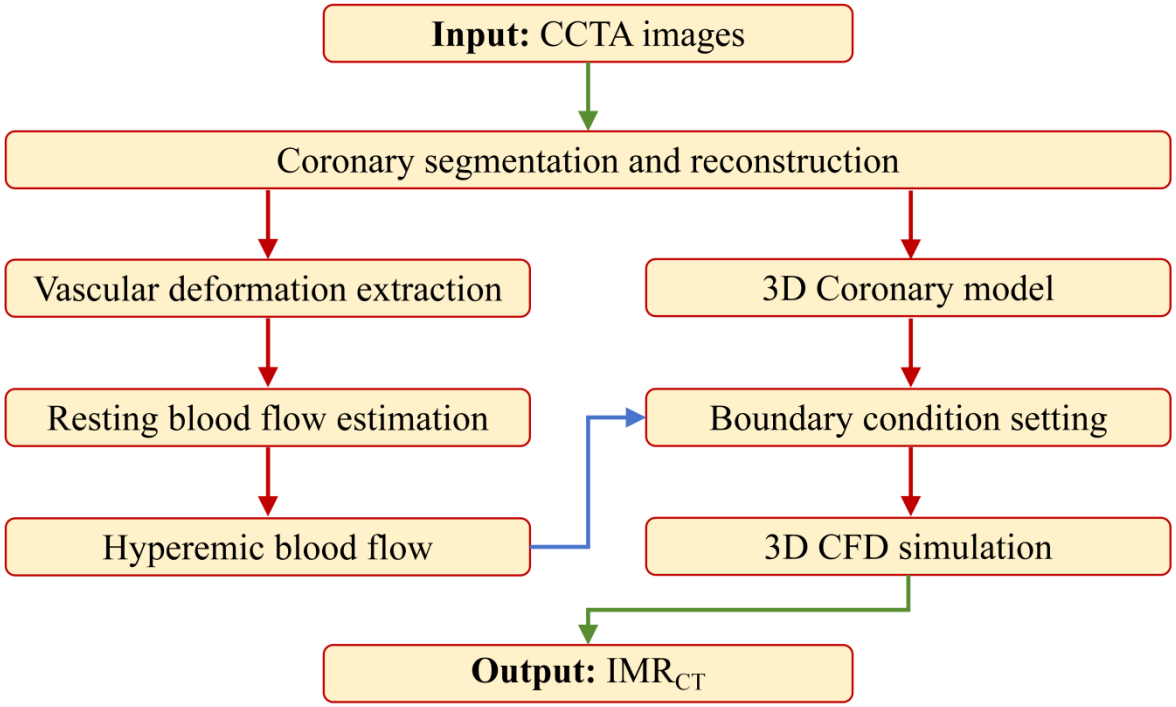

Supplementary Figure 1. Simplified schematic of the IMR_{CT} computational pipeline.

The workflow begins with coronary segmentation and 3D reconstruction from CCTA images. Vascular deformation is extracted from CCTA images to estimate hyperemic CBF, which is used for outlet boundary condition assignment. A patient-specific 3D model and defined boundary conditions are then used to perform CFD simulation, from which IMR_{CT} is computed. CCTA: coronary computed tomography angiography; CFD: computational fluid dynamics; CBF: coronary blood flow; IMR_{CT} = CCTA-based index of microcirculatory resistance.

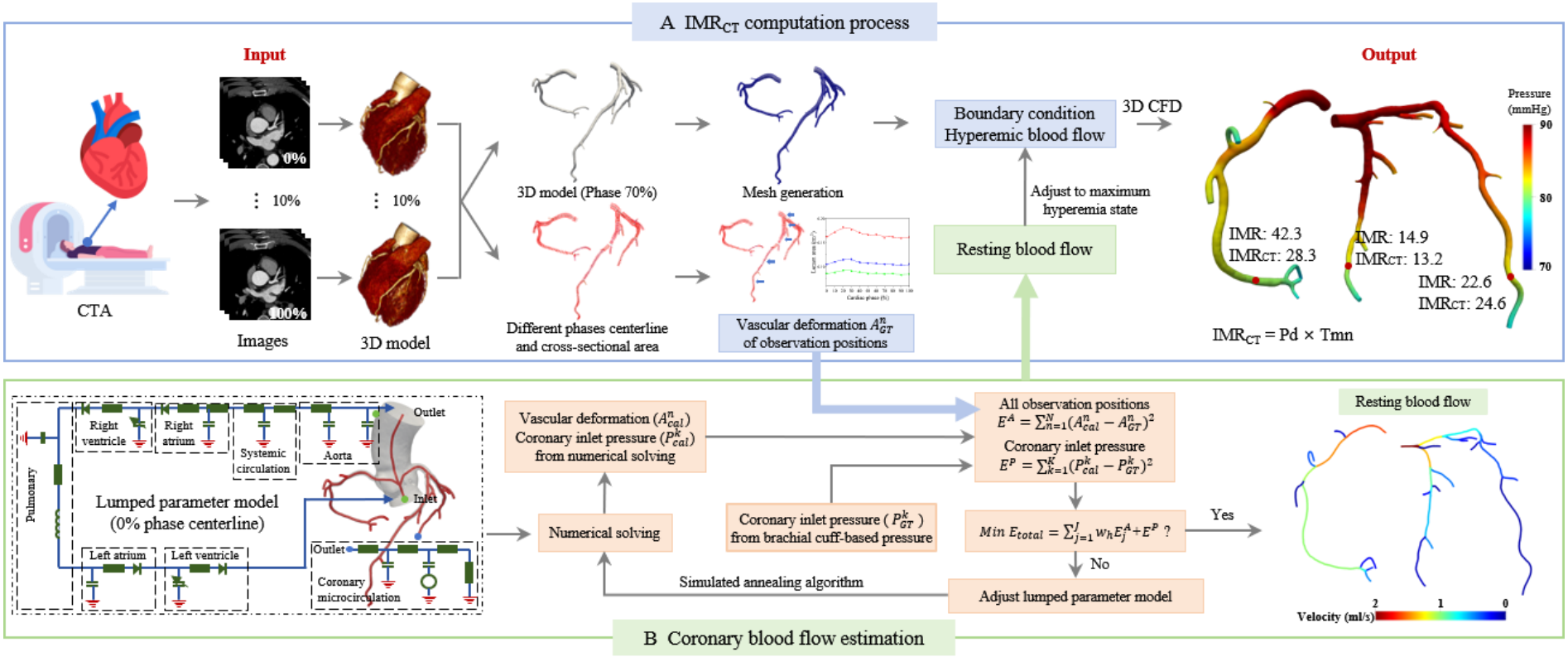

Supplementary Figure 2. Workflow diagram of the IMR_{CT} model.

A For each patient, the IMR_{CT} computational model takes CCTA images as input and outputs the IMR_{CT} value to detect coronary microcirculatory dysfunction. B By applying the concept of inverse problem solving, the coronary blood flow is implicitly derived based on the physical constraint relationship between blood flow and vascular deformation. CCTA: coronary computed tomography angiography; IMR_{CT}: CCTA-based index of microcirculatory resistance.

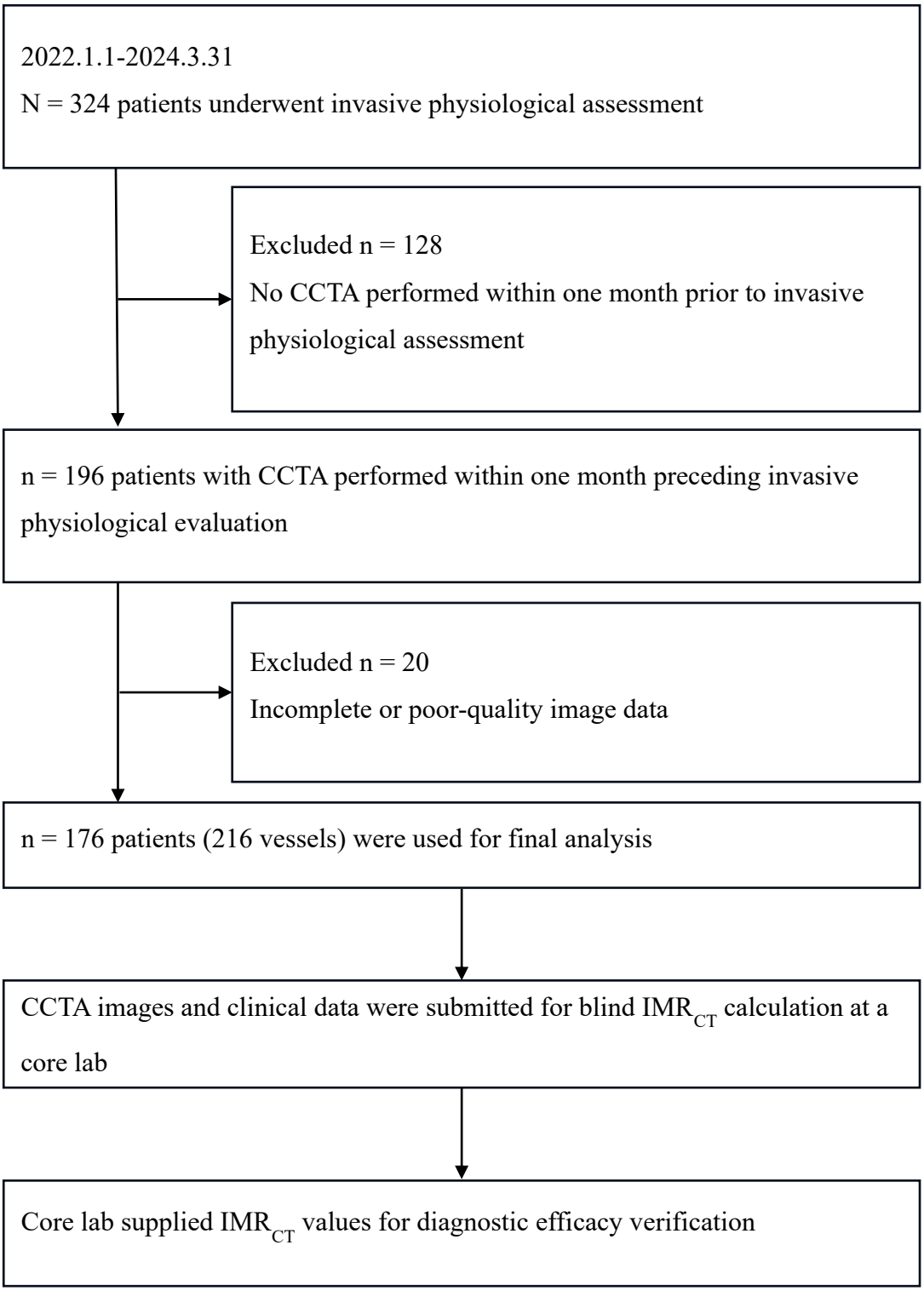

Supplementary Figure 3. Study flowchart.

CCTA: coronary computed tomography angiography. IMR$_{CT}$: CCTA-based index of microcirculatory resistance.

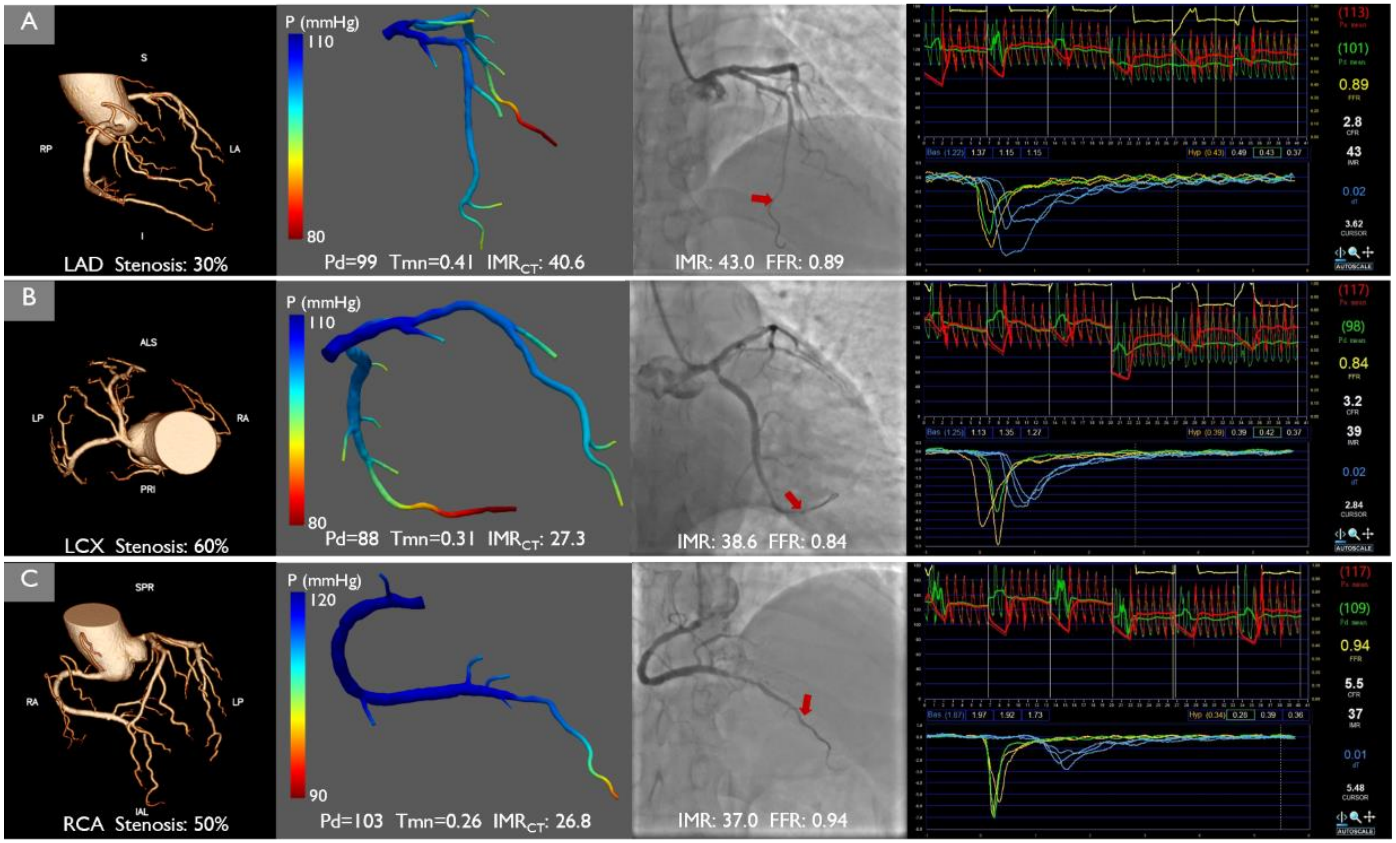

Supplementary Figure 4. Examples of IMR_{CT} computations for case 42, wherein all three coronary vessels exhibited concordant IMR values. In A to C, the images are arranged from left to right as follows: the CCTA volume-rendered image, IMR_{CT} computation result, CAG image, and invasive functional examinations. In the third column, invasive IMR measurements were adjusted according to Yong's formula when the FFR was ≤0.80. CAG: coronary angiography; CCTA: coronary computed tomography angiography; FFR: fractional flow reserve; IMR: index of microcirculatory resistance; IMR_{CT}: CCTA-based index of microcirculatory resistance.

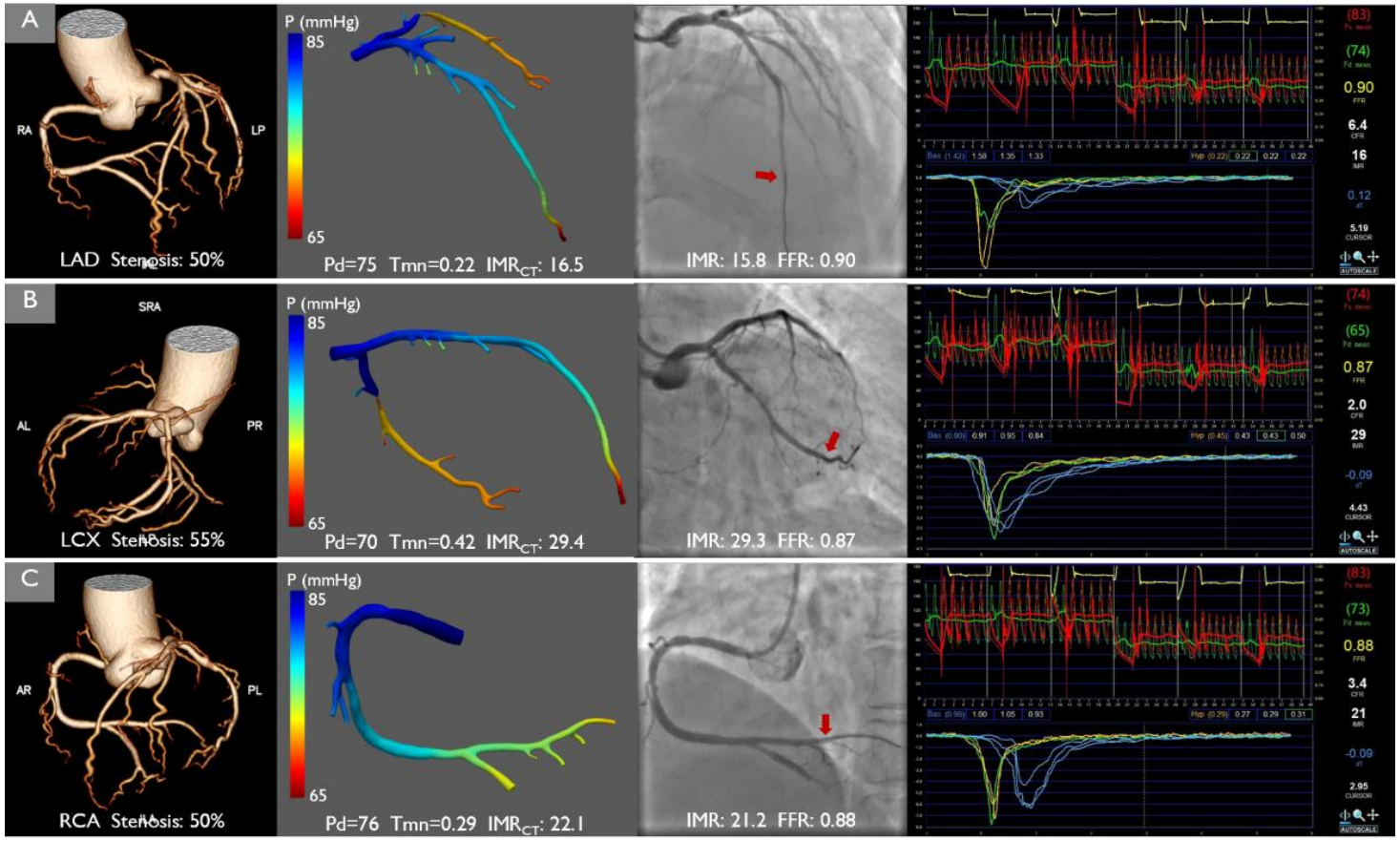

Supplementary Figure 5. Examples of IMR_{CT} computations for case 128, wherein all three coronary vessels exhibited discordant IMR values. In A to C, the images are arranged from left to right as follows: the CCTA volume-rendered image, IMR_{CT} computation result, CAG image, and invasive functional examinations. In the third column, invasive IMR measurements were adjusted according to Yong's formula when the FFR was ≤0.80. CAG: coronary angiography; CCTA: coronary computed tomography angiography; FFR: fractional flow reserve; IMR: index of microcirculatory resistance; IMR_{CT}: CCTA-based index of microcirculatory resistance.

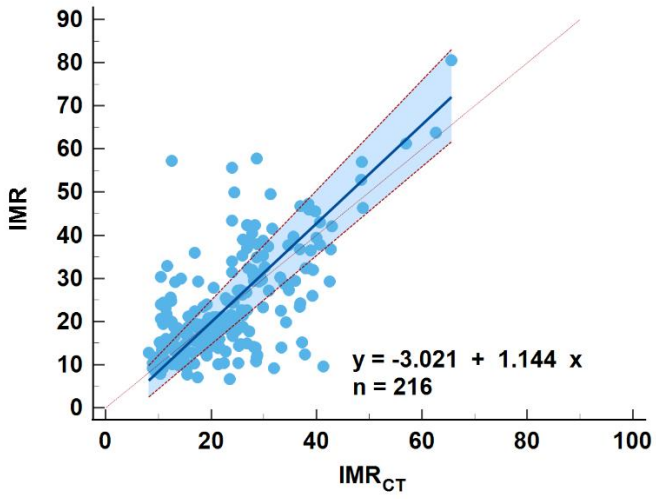

Supplementary Figure 6. Passing-Bablok regression analysis between IMR_{CT} and invasive IMR measurements.

The solid line represents the regression line (IMR = –3.02 + 1.14 × IMR_{CT}), with 95% confidence bands shaded. A dashed line indicates the line of identity (y = x). Regression parameters: intercept = –3.02 (95% CI: –5.91 to –0.59); slope = 1.14 (95% CI: 1.03–1.28). IMR: index of microcirculatory resistance; IMR_{CT}: CCTA-based index of microcirculatory resistance.

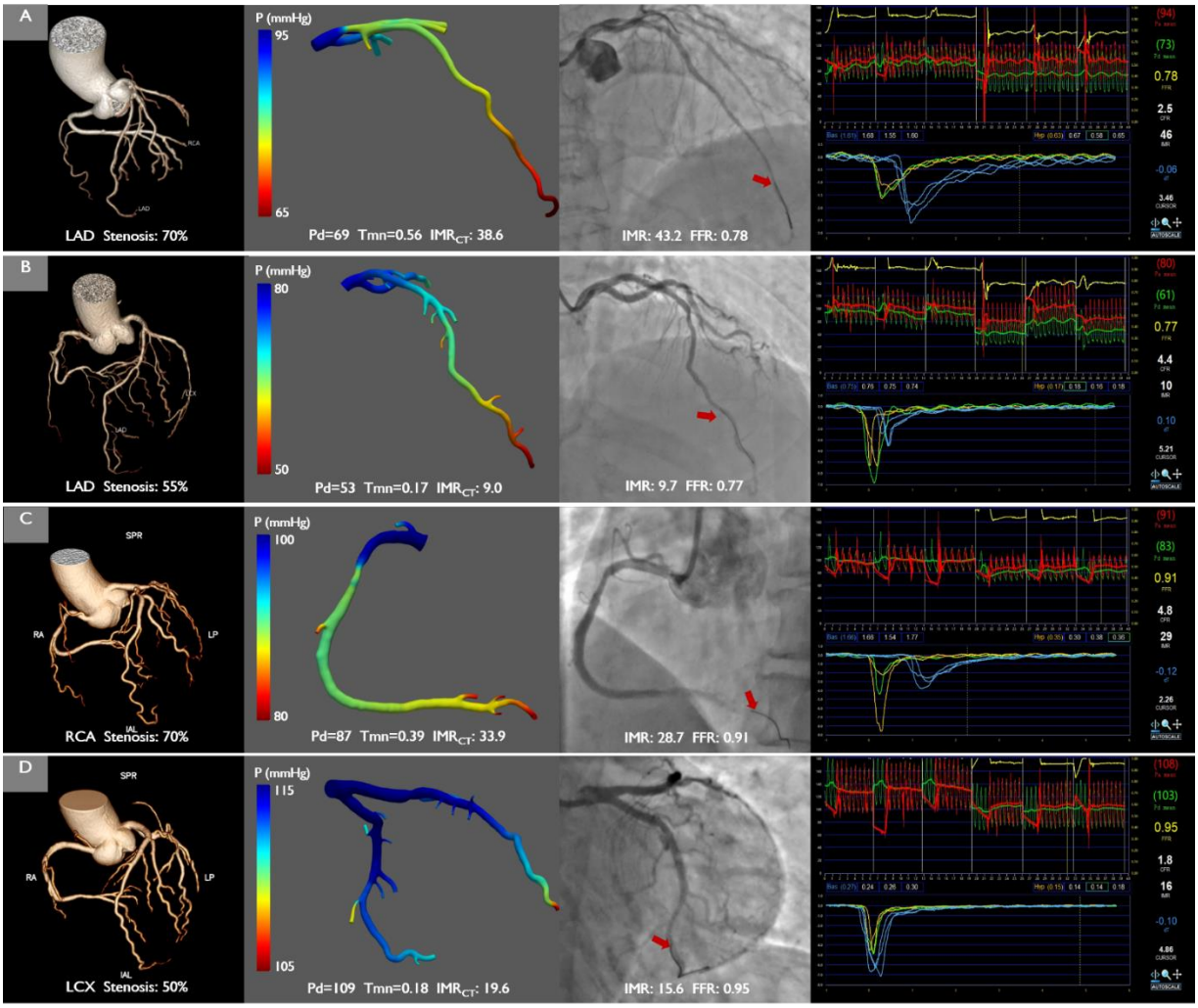

Supplementary Figure 7. Examples of IMR_{CT} computation under different physiological scenarios.

In A to D, the images are arranged from left to right as follows: the CCTA volume-rendered image, IMR_{CT} computation result, CAG image, and invasive functional examinations. In the third column, invasive IMR measurements were adjusted according to Yong's formula when the FFR was ≤0.80. CAG: coronary angiography; CCTA: coronary computed tomography angiography; FFR: fractional flow reserve; IMR: index of microcirculatory resistance; IMR_{CT}: CCTA-based index of microcirculatory resistance.

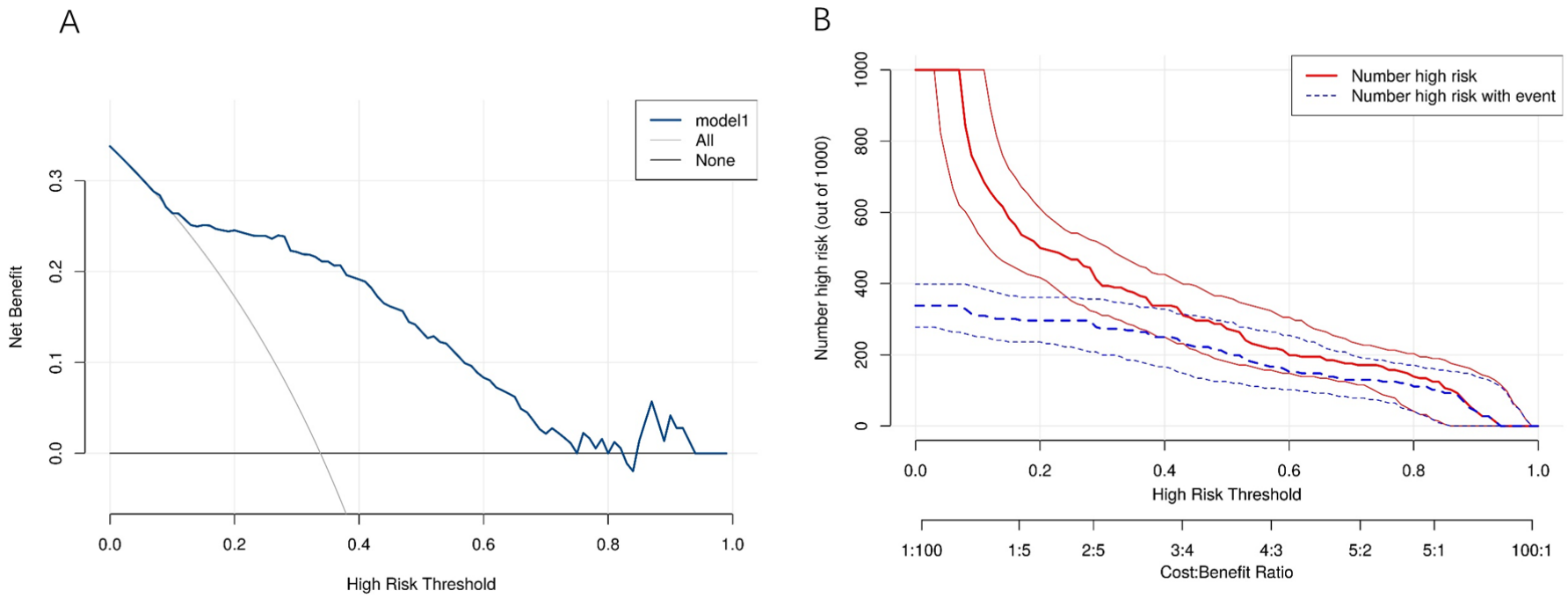

Supplementary Figure 8. Decision curve analysis of the IMR_{CT}-based predictive model.

A: Decision curve analysis demonstrates the clinical utility of the IMR_{CT}-based predictive model (Model 1). The x-axis represents the threshold probability for classifying patients as high risk (range: 0 to 1), and the y-axis shows the corresponding net benefit. Solid blue line: net benefit of Model 1; light gray dashed line: net benefit assuming all patients are classified as high risk ("All"); dark gray solid line: net benefit assuming no patients are classified as high risk ("None"). B: Model performance across varying cost:benefit ratios (range: 1:100 to 100:1). The x-axis indicates the cost:benefit ratio, and the y-axis shows the number of high-risk patients per 1000 individuals. Solid red line: total number of patients classified as high risk; dashed blue line: number of high-risk patients who experienced an event. IMR_{CT}: CCTA-based index of microcirculatory resistance.